A Numerical Investigation on High-Reynolds-Number Gravity Currents in Pressurized and Free-Surface Systems using Shallow Water Equation and Integral Model Approaches

by

Thomas Meyer Hatcher Jr.

A dissertation submitted to the Graduate Faculty of
Auburn University
in partial fulfillment of the
requirements for the Degree of
Doctor of Philosophy

Auburn, Alabama
December 13, 2014

Keywords: Gravity Currents, Lock-Exchange, Finite Volume Method, Shallow Water Equations, Integral Model

Approved by

José Goes Vasconcelos Neto, Chair, Assistant Professor of Civil Engineering
T. Prabhakar Clement, Professor of Civil Engineering
Xing Fang, Professor of Civil Engineering
Jay M. Khodadadi, Alumni Professor of Mechanical Engineering

Abstract

Multiphase flows in the form of gravity currents are prevalent in various natural systems, as well as in some open channels and closed conduits. These types of flow generally propagate in a horizontal direction playing an important role in contaminant transport, thunderstorms and pressure surge fluctuation in closed conduits. Thus, accurate flow simulation and efficient modeling tools are important in such applications. Laboratory experiments and numerical models are utilized in this work to study different types of gravity currents focusing on the lock-exchange problem. Both Boussinesq and non-Boussinesq flows are analyzed in the context of high-Reynolds number gravity currents. The numerical modeling efforts focus on solving the shallow water equations for Boussinesq gravity currents. In addition, an integral model is proposed for non-Boussinesq flows in closed conduits, and a Reynold-averaged Navier-Stokes model was developed in OpenFOAM for selected flow cases to compare model accuracy and computational efficiency.

Experiments were conducted alongside numerical model simulations for numerical validation and to analyze internal velocities that were measured with MicroADV devices. In previous research investigations, gravity current experiments focused on front trajectory, average depth, mixing, etc. by adjusting initial conditions (e.g. initial gravity current depth, inlet velocity, density difference, etc.). For physical modeling of gravity currents, the lock-exchange problem is often selected due to its simplicity, yet it has the ability to generate complex flow features characteristic of a broad range of gravity currents. Internal velocities had not been directly measured using MicroADVs for lock-exchange experiments, so numerical model calibration has focused on depth measurements and front velocities. Two MicroADV probes that measured velocities in both fluid layers are utilized in this work to

overcome this gap in experimental data. The MicroADV probes are utilized at three different depths by adjusting wooden supports. Results indicate that the difference in velocities caused by adjusting the vertical position of the ADVs is negligible within each fluid layer.

Using these velocity measurements, depth-averaged velocity hydrographs were obtained. A two-layer shallow water equation model was developed, which predicted these velocity hydrographs and gravity current front trajectories with fairly good accuracy. The proposed model differs from existing approaches in that it utilizes shock-capturing theory in a finite volume framework to seamlessly predict shocks that develop in lock-exchange problems. This feature allows for simpler numerical implementation particularly when the direction of these flow discontinuities is unknown apriori.

Another two-layer shallow water equation model was developed for a similar case in which the lighter ambient fluid was not initially stagnant. This shock-capturing model was tested with [Wright and Paez-Rivadeneira, 1996] experiments and [Hallworth et al., 1998] numerical model for ambient flows moving with (coflows) and against (counterflows) the gravity current. Model results compare well with the shock-fitting model of [Hallworth et al., 1998] while using a simpler numerical implementation. For the lock-exchange problem, the proposed SWE model is the first approach tested with nonlinear numerical schemes, to the best of our knowledge. The quantitative difference in results produced by linear and nonlinear numerical schemes is negligible unless small Courant numbers are expected in model simulations. The HLL Riemann Solver is used throughout this work in which model results compare well with shock-fitting alternatives in resolving flow discontinuities.

One of the challenges in shallow water equation models applied to gravity currents is the requirement that a boundary condition is needed at the leading edge. Existing methods utilize the method of characteristics in which the characteristic expressions and numerical implementation can change for different flow cases increasing modeling complexity. In addition, systematic guidelines had not been provided for boundary condition implementation in different flow scenarios. A new boundary condition approach is proposed in this work that

is applicable for one- and two-layer SWE models with two computational cells utilized at the gravity current leading edge. Boundary condition implementation is identical for both SWE models. Similar to the solution approach by [Li and McCorquodale, 1999] applied to air-water flows in storm sewers, this method enforces local continuity and momentum. Alternatives employing the method of characteristics are systematically compared with the proposed boundary condition in terms of ease of implementation, continuity errors and computational efficiency. Results indicate that the proposed method is a good compromise for the tested flow conditions.

Non-Boussinesq gravity currents are also investigated in this dissertation focusing on air-water interactions in closed conduits. When air becomes entrapped in storm sewers during intense rain events, pipelines may experience pressures much greater than driving pressure heads [Martin, 1976]. These air pockets may propagate in the form of non-Boussinesq gravity currents and can lead to structural damage through urban geysering [Vasconcelos, 2005]. Although the prediction of air pocket location is important, numerical models applied to multiphase flows in storm sewers do not account for the motion of air. Instead of resolving the free-surface interface, an integral model is proposed to simulate air pocket motion that assumes uniform air pocket depth. This new approach builds on the work of [Benjamin, 1968] and [Wilkinson, 1982] in which a known quantity of air is suddenly released in a closed conduit. The integral model was tested with a large range of air pocket volumes and background flow velocities in experiments conducted by [Chosie, 2013] using $D = 101.6$ mm pipes. Results indicate that air pocket velocities are predicted with an average error of 4% or less. An extension to favorable and adverse slopes is expected in future extensions of the proposed integral model.

Acknowledgments

I would like to thank my advisor, Professor Jose Goes Vasconcelos, for his experience, hard work and friendship throughout my time at Auburn and hopefully long into the future. He introduced me to experimental and numerical hydraulics and was instrumental in the development of this dissertation. I also received a great deal of help from my fellow students. Bernardo Trindade and Gabriel Leite helped introduce me to numerical modeling and their friendship played an important role in my graduate work. Parker Ross assisted in the construction of the physical model used in gravity current experiments. Andrew Patrick, Kyle Moynihan and Kyle Strachan, Carmen Chosie and Paul Simmons also helped with experimental hydraulics.

My family played an important role in the development of this dissertation with all of their support the last four years and throughout my life. My best friend and wife, Jennifer Kelly Hatcher, has been the centerpiece in my life these last few years and has provided essential love and support. My parents, Tom and Sharon Hatcher, have provided incredible support throughout my life. I could not have asked for better role models. I would like to congratulate my brother, Preston Hatcher, for winning the career saves record at Western Carolina and thank him for teaching me self control as a child. Finally, I would like to thank all of my friends in the engineering department who helped make my time at Auburn enjoyable.

Table of Contents

List of Figures

List of Tables

List of Notations

The following symbols are used in this dissertation:

Fr_{H}	=	Total depth densimetric Froude number
Fr_{LE}	=	Froude number at the GC leading edge
g'	=	Reduced gravitational acceleration = $g\epsilon$
h_0	=	Initial depth of denser fluid
h, h_1	=	Depth of GC
h_2	=	Depth of ambient fluid
h_{ADV}	=	Depth of the MicroADV probe
h_{LE}	=	Depth of leading edge or front of GC
H	=	Initial ambient depth, total depth of system
Re	=	Reynold's number
Re_{m}	=	Mean Reynold's number
u, u_1	=	Velocity of GC
u_2	=	Velocity of the ambient fluid
u_{LE}	=	Velocity of the GC leading edge
u_{m}	=	Mean velocity at the GC front
x_0	=	Initial length of denser fluid
β	=	Scaling factor for the front condition
ϵ	=	Relative density difference = $(\rho_c - \rho_a)/\rho_c$
ρ_c, ρ_1	=	Density of bottom GC
ρ_a, ρ_2	=	Density of ambient fluid
$\Delta\rho$	=	Difference between the current and ambient densities = $\rho_c - \rho_a$
ϕ	=	Initial depth ratio or fractional depth = h_0/H
ϕ_{LE}	=	Depth ratio of the GC leading edge

$\vec{U}$	=	Vector of conserved variables
$F(\vec{U})$	=	Vector of conserved variables fluxes
$S(\vec{U})$	=	Vector of source terms
A, B	=	Source term parameters
Δx	=	Dimension of space discretization
Δt	=	Dimension of time discretization
$k_{\Delta t}$	=	Scaling factor for time step calculation
Cr	=	Courant number
DC	=	Dual-Cell
GOC	=	Grid-Of-Characteristics
MOC	=	Method of Characteristics
STI	=	Specified Time Intervals
$RANS$	=	Reynolds-Averaged-Navier-Stokes
ϵ	=	Turbulent dissipation
k	=	Turbulent kinetic energy
$k-\epsilon$	=	$k-\epsilon$ RANS turbulent model
υ	=	Turbulent stress normal to streamlines
$\overline{\upsilon^2}-f$	=	$\overline{\upsilon^2}-f$ RANS turbulent model

Chapter 1

Background

The mixing and motion of Boussinesq fluids ($\rho_1/\rho_2 \approx 1$) in inland waterways are widely studied phenomena in which temperature, contaminant transport, etc. are significantly affected. These flows often resemble gravity currents, which generally flow in a quasi-horizontal plane with buoyancy comparable to or greater than other relevant forces (e.g. inertia, viscosity and/or surface tension). Examples of such flows include saltwater intrusions in estuaries and thermal discharges in rivers (e.g. warmer wastewater effluent entering colder river bodies). Non-Boussinesq gravity currents, on the other hand, may appear in storm sewers during intense rain events in which the presence of moving air pockets may lead to loss of conveyance, structural damage and/or geysering [Vasconcelos, 2005]. These gravity current (GC) flows may also be present in other applications including pipeline priming and normal operation of force mains. This work will focus on high-Reynolds number gravity currents flowing in a prismatic channel/pipe with and without ambient crossflows.

This investigation explores selected aspects of inviscid GC flows in the context of civil and environmental engineering applications. Experiments were performed primarily for Boussinesq fluids focusing on the numerical solutions of lock-exchange problems. Boussinesq fluids possess similar densities (e.g. less than 2.0%), which mathematically simplify the governing equations as described ahead in this dissertation. The numerical modeling effort in this work focused on the shallow water equations (SWE), but more sophisticated computational fluid dynamics (CFD) models were developed in OpenFOAM to assess model accuracy. Non-Boussinesq (e.g. air and water) experiments were also conducted with the objective of understanding air pocket kinematics and involved the entrapment and release

of air pockets within steady closed pipe flows. These experiments were accompanied by a numerical model applying the integral model approach.

The prediction and modeling of GC flows generally follow three approaches: integral, shallow water equation and Navier-Stokes equation (NSE) models. The following sections review the applications of experiments and numerical models for Boussinesq and non-Boussinesq gravity currents.

- First, experimental contributions are provided for Boussinesq GC flows focusing on the lock-exchange problem.
- One-layer shallow water equations (SWE) are introduced for Boussinesq and non-Boussinesq applications.
- The two-layer SWE are analyzed for Boussinesq systems with and without ambient crossflows.
- Leading edge boundary condition (BC) solution alternatives are analyzed for one- and two-layer SWE models.
- Finally, non-Boussinesq air-water gravity currents are explored with a computationally efficient integral model approach.

1.1 Gravity current experimental investigations

Along with analytical and numerical research, experimental investigations have provided important insights into GC flows. [Simpson and Britter, 1979] studied a large range of fractional depths/depth ratios ($\phi = h_0/H$) for GC flows and determined the respective dimensionless velocities, rate of mixing, and depth of the mixed layer behind the head. Their apparatus consisted of a moving floor and a downstream weir, which allowed them to halt the GC flow in order to obtain more accurate measurements. A similar procedure

was utilized by [Wright and Paez-Rivadeneira, 1996] to analyze the effects of coflows and counterflows in which the ambient water is flowing with or against the GC, respectively.

In their lock-exchange experiments (see 1.1), [Rottman and Simpson, 1983] analyzed a large range of ϕ and compared the results with a two-layer SWE model. Using large initial depths, [Rottman and Simpson, 1983] concluded experimentally that the upstream moving hydraulic jump generated upon gate removal occurs when $\phi \geq 0.7$. Once this disturbance reflects off of the upstream boundary a hydraulic drop is formed that eventually overtakes the GC front marking the beginning of the self-similar stage. For smaller fractional depths, the upstream moving jump is replaced by a depression wave [Rottman and Simpson, 1983].

In [Hacker et al., 1996] a digital image technique (DigImage, [Dalziel, 1993]) was used to determine the density structure for lock-release GC flows. They were able to observe the detrainment of dense fluid at the GC nose caused by breaking Kelvin-Helmholtz waves, which produced a stratified region behind the nose. This diluted fluid in this region was replaced by dense fluid behind the nose, which traveled toward the front of the GC. Thus, this process leads to re-circulation that causes the entire GC to become diluted. [Hacker et al., 1996] utilized the total depth densimetric Froude number (Fr_{H}) and the mean Reynolds number

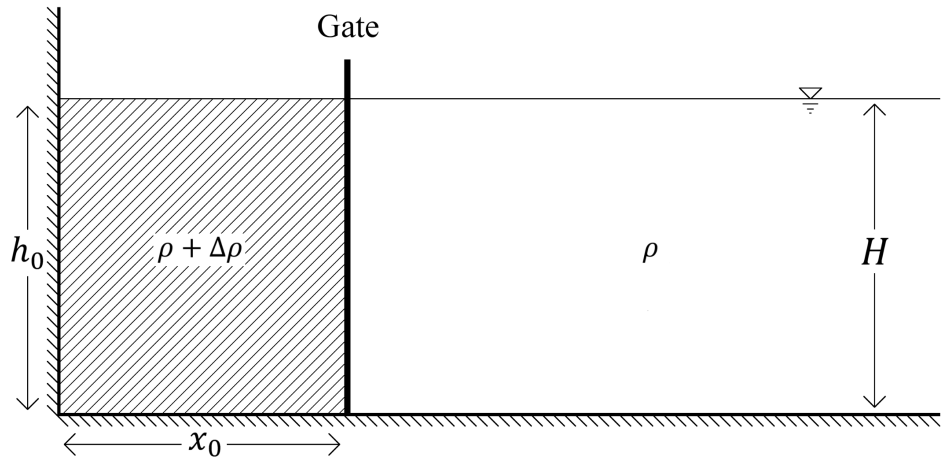

Figure 1.1: Schematic diagram of lock-exchange problem

(Re_m) to analyze gravity currents with different mixing rates:

$$Fr_{\mathrm{H}} = \frac{u_{\mathrm{m}}}{\sqrt{h_0\, g'}} \qquad\qquad Re_{\mathrm{m}} = \frac{1}{2}\frac{u_{\mathrm{m}}\, h_0}{\nu} \tag{1.1}$$

where h_0 is the initial depth of the denser fluid, g'_0 is the initial reduced gravity, u_{m} is the mean velocity of the GC front and ν is the kinematic viscosity. Re_{m} is multiplied by $\frac{1}{2}h_0$ because this is the energy conserving depth described by [Benjamin, 1968]. These dimensionless parameters are provided for the experiments in section 3.1.2.

Numerous experimental investigations have utilized sodium chloride (NaCl) in their experiments to generate Boussinesq GC flows ([Rottman and Simpson, 1983], [Shin et al., 2004], etc.). The same approach was implemented in the experiments presented in this work. For non-Boussinesq lock-exchange flows, [Lowe et al., 2005] used sodium iodide (NAI) in addition to NaCl in order to obtain density ratios (ρ_2/ρ_1) between 0.6 and 1.0. From their non-Boussinesq experiments, they determined that in most cases the lighter current retains its energy-conserving depth while the denser current is dissipative, so the depth decreases at a rate that depends on the density ratio.

[Gerber et al., 2011] used a particle image velocimetry (PIV) to measure the Reynolds stress and shear production of turbulence of a stably stratified GC. Their experimental results compared well to their Reynold's averaged NSE numerical model. [Firoozabadi et al., 2010] used Micro Acoustic Doppler Velocimeter (MicroADV) probes to measure the turbulence energy, Reynolds stresses and turbulence intensity of 3-D GC flows for various flow rates, concentrations and slopes. As the discharge and the concentration increased, the turbulence kinetic energy also increased. Their results also indicate that the normalized turbulence intensity does not change with bed slope.

1.2 Shallow water equation modeling for Boussinesq gravity currents

There are two primary SWE modeling alternatives to simulate gravity currents: one-layer and two-layer. In deep ambient conditions, the displacement of a dense layer along the bottom of the solution domain (or conversely a lighter layer on the top) will not create significant counter currents and thus its motion is unaffected by the ambient flow, a case analogous to a dam-break flow. These cases are well represented by the one-layer SWE model, but this modeling approach is not applicable in the case of lock-exchange GC flows. Significant counter currents may develop following the gate removal when the initial fractional depth ($\phi = h_0/H$) approaches 0.5, causing significant deviation between one-layer SWE model predictions and experimental observations. For such cases, it is very important to incorporate ambient layer effects into GC motion using a two-layer SWE model.

In a wide range of hydraulic applications, numerical models have employed shock-capturing approaches based on the Riemann problem. Examples of recent works using these finite volume method (FVM) approaches include: channels with irregular geometry [Elena and Vazquez-Cendon, 1999], shallow water flows with topography [Gallouet et al., 2003], stormwater tunnels [Vasconcelos and Wright, 2006], pollutant transport [Benkhaldoun et al., 2007], dam breaks with wetting and drying [Liang and Marche, 2009], etc. Numerical models used in these works have performed well in resolving shocks, which are expected for the lock-exchange problem. It was expected that these conservative approaches would perform better for GC flows than existing modeling techniques, so shock-capturing approaches are extended to GC applications in this work.

1.2.1 One-layer shallow water equation modeling

In GC flow applications, one-layer SWE models are employed when the GC depth is significantly less than the ambient flow depth ($h_0/H \leq 0.5$). In contrast with the two-layer SWE, the ambient fluid velocity is neglected in the GC momentum formulation. Both one and two-layer SWE models can provide an accurate estimation of the GC front and

are computationally efficient compared to the more complex Navier-Stokes models. In the following text, the details of the one-layer SWE model are analyzed and several of the important research investigations are included.

One-layer SWE models have been widely used for gravity currents flowing into deep ambient fluids with key advantages being simplicity and computational efficiency. Because the velocity of the ambient fluid is neglected, discontinuous solutions are generally not observed for prismatic channel flows but may be present when obstacles or complex geometries exist. Details of the one-layer formulation are found in [Ungarish, 2009] for both Boussinesq and non-Boussinesq fluids. In this section the focus is on Boussinesq fluids; however, it is relatively simple to expand the one-layer model to non-Boussinesq flows. Therefore, the more generalized one-layer, non-Boussinesq SWE model is utilized in this work [Ungarish, 2007]:

$$\frac{\partial h}{\partial t} + \frac{\partial uh}{\partial x} = 0 \tag{1.2}$$

$$\frac{\partial uh}{\partial t} + \frac{\partial}{\partial x}\left(\frac{(uh)^2}{h} + \frac{1}{2}g'h^2\right) = 0 \tag{1.3}$$

where h and uh are the depth and flow rate per unit width of the GC, respectively. $g' = [(\rho_c - \rho_a)/\rho_c]\, g = \epsilon g$ is the reduced acceleration due to gravity in which ρ_c and ρ_a are the density of the current and ambient fluids, respectively; ϵ is the relative density difference.

[Ungarish, 2007] implemented the one-layer SWE model for a large range of depth ratios and density differences. Boussinesq GC flows were analyzed for the lock-exchange problem as a special case of non-Boussinesq flows. Although there are several important underlying assumptions in this approach, the generality, absence of empirical coefficients and computational efficiency make the one-layer model an attractive modeling choice [Ungarish, 2007]. [Hallworth et al., 1998] and [Hogg et al., 2005] extended the one-layer SWE model to particle-driven gravity currents propagating in the presence of a uniform ambient flow for constant-volume and constant-flux cases, respectively. [Ungarish and Huppert, 2004] applied this SWE model to gravity currents traveling at the base of a stratified ambient and

determined that the stratification reduces the GC velocity. Thus, the one-layer alternative can be applied to a wide variety of flow scenarios.

Because the ambient fluid momentum is neglected in the GC momentum expression (Eq. 1.3), there are important limitations for the one-layer SWE model that are highlighted when simulating gravity currents with large depth ratios. For example, as ϕ increases beyond 0.5, the depression wave generated upon gate release transitions into a hydraulic jump-like feature [Ungarish, 2009]. The one-layer model cannot simulate this feature or the change in depth that accompanies this jump. To avoid these potential errors, two-layer SWE models became popular in the last few decades as discussed in the following subsection.

However, [Ungarish, 2007] proved that the one-layer SWE model is useful for lock-exchange simulations when used in the correct context. Although the one-layer model is unable to accurately simulate the depth profile particularly at the initial flow stages, the GC leading edge trajectory is accurately simulated throughout the initial slumping stage and into the self-similar stage without the use of empirical coefficients [Ungarish, 2007]. For the lock-exchange problem, the error between measured and simulated GC front trajectories is approximately 3% using the one-layer SWE model [Hatcher, 2012]. The models surprising accuracy for the lock-exchange problem is more than likely caused by a fortunate balance of errors from different simplifications [Ungarish, 2007]. The ambient fluid velocity increases the GC velocity in the lock-exchange problem, but this increase is balanced by the reduction in velocity due to entrainment. The single-layer SWE model cannot simulate either one of these complex flow features, but the combined effect of neglecting them leads to an accurate estimation for the GC front trajectory. As ϕ decreases, this error balance changes, and the accuracy of the one-layer model for GC front trajectories also decreases despite being more theoretically sound [Ungarish, 2007].

To simulate gravity currents with SWE, numerical solutions are required. Analytical solutions exist for the initial slumping stage and later stages of the flow, but the transition

between flow stages cannot be simulated analytically. For two-layer SWE models, no analytical solutions exist [Ungarish, 2009]. Prior to this work, lock-exchange gravity currents have only been solved numerically using the method of characteristics (MOC) and the Finite Difference Method (FDM) in the context of SWE models. When discontinuities are not expected, the MOC is a popular modeling choice. The characteristic equations for the one-layer SWE model are presented in [Ungarish, 2007]:

$$g'^{\frac{1}{2}} \frac{dh}{h^{1/2}} \pm du = 0 \qquad \text{on} \quad \frac{dx}{dt} = u \pm (g'h)^{1/2} \tag{1.4}$$

in which the second expression represents the characteristic flow velocities. Although these equations (1.4) can be used to compute the internal cell calculations, [Ungarish, 2007] implemented the Lax-Wendroff two-step FDM scheme to solve Eqs. 1.2 and 1.3. This numerical scheme is well documented and performs well in the absence of shocks [Chaudhry, 2008], which are generally not present in the one-layer model. The MOC was used in the BCs of the [Ungarish, 2007] simulations. The implementation of such BCs are highlighted in Section 1.3.

1.2.2 Two-layer shallow water equation modeling

Two-layer SWE are comprised of four partial differential equations (PDEs) that represent mass and momentum conservation in both fluid layers of different densities [Rottman and Simpson, 1983]. Two-layer models are most often implemented for the release of dense fluids into relatively small ambient depths (e.g. the lock-exchange problem). [Rottman and Simpson, 1983] developed the first two-layer SWE model for GC flows in the context of partial-depth releases. By adopting some simplifying assumptions (e.g. Boussinesq fluids, depth uniformity, etc.) they were able to reduce the problem to a system of two PDEs describing the dense layer and to develop a solution via characteristic analysis, yielding the

following system of ODEs:

$$\begin{aligned} h\frac{du}{dh} - (1-2a)u + c_{\pm} &= 0 \\ c_{\pm} = u(1-a) \pm \left[u^2a^2 + g'h(1-b)\right]^{1/2} & \end{aligned} \tag{1.5}$$

in which $u = q/h = uh/h$ is the velocity of the GC layer. The parameters a and b were formulated in the two-layer formulation by [Rottman and Simpson, 1983] and are discussed in the Methodology section.

While numerical simulations based on MOC have been applied successfully in a number of unsteady flow applications, these models break down when characteristic lines of the same family intercept one another [Chaudhry, 2008]. The [Rottman and Simpson, 1983] two-layer SWE model presents non-physical results when $\phi \geq 0.5$ in the form of a multi-valued solution for depth (h). Experimental observations performed by [Rottman and Simpson, 1983] indicate that such conditions correspond to regions with sharp gradients at the interface between fluids and form when $\phi \geq 0.7$, instead of 0.5, due to viscous effects. Thus, an accurate representation of lock-exchange flows require special handling of these discontinuities either by explicit tracking [Klemp et al., 1994, Ungarish and Zemach, 2005] or by shock-capturing techniques as presented in this work.

[Klemp et al., 1994] extended the two-layer model implemented by [Rottman and Simpson, 1983] in order to simulate lock-exchange gravity currents for $\phi > 0.5$. Instead of using MOC, [Klemp et al., 1994] implemented a FDM model using the second-order accurate Leapfrog scheme [Cunge et al., 1980]. [Ungarish and Zemach, 2005] extended the works of [Rottman and Simpson, 1983] and [Klemp et al., 1994] in order to simulate the entire slumping stage, which ends when the GC leading edge propagates approximately 10 lock lengths ($x_{LE} \approx 10x_0$) [Rottman and Simpson, 1983]). The FDM model used the second-order accurate Lax-Wendroff (LxW) numerical scheme and performed explicit tracking of flow discontinuities. These shocks were treated as depth discontinuities in a way that resembles the shock-fitting approach used to track open channel bores [Cunge et al., 1980].

More recently, [Adduce et al., 2012] formulated an alternative two-layer SWE model that incorporates entrainment. The conserved variables in their model were $\rho_1 h_1$, $\rho_2 h_2$, u_1 and u_2. Instead of focusing on the simulation of shocks, [Adduce et al., 2012] analyzed the effects of entrainment and shear forces, which decrease the GC front velocity.

In numerous flow applications, existing ambient flows exist that cannot be neglected in SWE formulations (e.g. denser wastewater effluent released in a river). Most SWE models do not account for these ambient crossflows and assume stagnant initial conditions. [Hallworth et al., 1998] provided one of the first quantitative analyses on the effect of ambient crossflows in gravity currents and focused on three modeling approaches: integral models and the one-layer and two-layer SWE models. [Hogg et al., 2005] built on the work of [Hallworth et al., 1998] by expanding their modeling approaches to account for constant-flux intrusions. Both of their two-layer SWE models were not developed using a conservative modeling framework, so there are potential difficulties in the simulation of naturally occurring flow discontinuities, which are characteristic of hyperbolic PDEs. In [Hallworth et al., 1998] and [Hogg et al., 2005] simulations, shocks were avoided by utilizing small depth ratios ($\phi << 1$), but this assumption does not always hold in some applications. In section 3.2.3 a two-layer SWE model accounting for ambient crossflows is proposed for constant-volume gravity currents. The proposed SWE model is written in conservative format so that it is able to simulate shocks when ($\phi \leq 0.7$).

1.3 Alternatives for flow solution at the leading edge of gravity currents

One of the most widely studied components of GC flows involves the front condition that controls the GC depth and velocity. These front conditions, which range from theoretical [Benjamin, 1968, Shin et al., 2004] to empirical [Huppert and Simpson, 1980, Rottman and Simpson, 1983, Marino et al., 2005] approaches, are implemented in analytical and numerical models. In contrast with front conditions, the other component of the leading edge BC that brings information from the upstream side of the GC front has received little attention in

SWE models. Three front BC approaches have been formulated with two based on the MOC. One of the downsides of MOC-based approaches involves the complexity when the characteristic equations change. For example MOC expressions and, as a result, front BC approaches are different for one-layer and two-layer SWE models. In addition, it is difficult to determine the most appropriate method to implement based on the flow application. In a recent work, [Hatcher and Vasconcelos, 2013a] proposed a new method that conserves mass and momentum that uses the same implementation for a wide variety of GC flows.

SWE models require special handling at the leading edge of gravity currents since flow conditions there violate the assumptions used in these models. At the leading edge, there are strong vertical accelerations and mixing that contribute to a curved interface between GC and ambient fluids that invalidates some of the hypotheses formulated in the SWE derivation. To overcome the difficulties at these locations, SWE models adopt front conditions that relate the GC depth and correspondent velocity at the leading edge region. An early example of these front conditions was proposed by [von Karman, 1940]:

$$\frac{u_{\text{LE}}}{(g' h_{\text{LE}})^{1/2}} = Fr_{\text{LE}} \tag{1.6}$$

in which g' is the reduced gravity defined as $g' = \Delta\rho/\rho_0$, and u_{LE}, h_{LE} and Fr_{LE} are the velocity, depth and Froude number at the leading edge, respectively. Defining $\phi = h_0/H$ as the initial depth ratio between current and ambient fluids, Von Karman applied this front condition to the deep ambient scenario ($\phi \approx 0$) with $Fr_{\text{LE}} = \sqrt{2}$; [Benjamin, 1968] extended Eq. 3.25 to the range $0 < \phi \leq 1$ in a more comprehensive analysis. Because both of these theoretical front conditions overestimate the GC front velocity, significant research has focused on empirical front conditions that account for entrainment, friction, dissipation, etc. [Huppert and Simpson, 1980, Rottman and Simpson, 1983]. For the leading edge BC solution strategy comparison, the Huppert and Simpson front condition (referred to as *HS*)

is utilized where Fr_{LE} is computed from the following relationship:

$$Fr(\phi_{\text{LE}}) = \begin{cases} \frac{1}{2}\phi^{-\frac{1}{3}} & (0.075 \leq \phi_{\text{LE}} < 1) \\ 1.19 & (\phi_{\text{LE}} \leq 0.075) \end{cases} \tag{1.7}$$

The *HS* front condition has been tested with good accuracy for several types of GC flows [Ungarish, 2009]. For the two-layer SWE model presented in Section 3.2.2, a different method is used based on the pioneering work of [Rottman and Simpson, 1983]. Their front condition adjusts the theoretical model of [Benjamin, 1968] with an empirical parameter (β) to account for entrainment and friction:

$$Fr_{\text{LE}} = \frac{\beta}{\sqrt{2}} \left[\frac{(2 - \phi_{\text{LE}})(1 - \phi_{\text{LE}})}{1 + \phi_{\text{LE}}} \right]^{1/2} \tag{1.8}$$

For partial depth releases, [Rottman and Simpson, 1983] calibrated β to equal unity. $\beta = \sqrt{2}$ reproduces Benjamin's theoretical condition, but the resulting velocities are overestimated by approximately 20% for the lock-exchange problem due to the effects of entrainment. In this work β was re-calibrated for $\phi = 1$ scenarios to equal 1.21 based on experimental observations.

Regardless of the implemented front condition, there is one equation for the two unknowns (u_{LE} and h_{LE}, where $\phi_{\text{LE}} = h_{\text{LE}}/H$ at the GC leading edge), so another equation must be provided. A traditional method to provide this equation has been through the MOC, whereby a relevant characteristic equation that is valid within a trajectory in the space-time solution domain (a characteristic line) is used to provide closure to the flow calculation. Within the MOC, there are two alternatives to provide this equation:

- Grid-of-Characteristics (GOC): Described by [Lai, 1988], this method involves explicit tracking of characteristic lines to determine flow conditions at locations where they intercept each other or intercept a BC, such as GC leading edges.

- Specified time intervals (STI): Also known as Hartree MOC [Sturm, 2010], this popular approach involves back-projecting of characteristic lines in the space-time grid and spatial interpolation of variables between the leading edge coordinate and the adjacent node.

A third method referred to as Dual-Cell (DC) has been proposed by [Hatcher and Vasconcelos, 2013a] and attempts to provide a set of equations that ensure observance of continuity and momentum equations at the leading edge region. In addition to these equations, the DC method uses a front condition (e.g. Eqs. 3.25) and 1.7 to determine flows at the GC leading edge. This method has been proven accurate to simulate both one and two-layer SWE models when compared with experimental results presented by the authors. These comparisons involved constant-volume GC flows, but not constant-influx GC flows.

While there has been significant progress in the development of improved front conditions to simulate GC flows, a more detailed study on the advantages between the different leading edge BC solution strategies has not received as much attention. Some important questions are still open and require clarification. First, the STI approach is a practical and relatively cheap alternative to solve flows at GC leading edges, but one question is to what extent the interpolation it introduces affect simulation accuracy. Second, while the GOC approach does not use interpolation, a relevant question is how expensive is the explicit tracking of characteristic lines that were generated at the upstream BC, particularly for highly-discretized solution domains. Third, the relative performance of the DC method when compared to the MOC methods has not been assessed to this date. Finally, another pertinent question is whether there are applicability limits to the outlined strategies to solve flows at GC leading edge in the context of constant-volume and density intrusion GC. The main purpose of this work is to address these questions.

1.4 Air pocket motion in closed conduits

Intense rain events in urban areas lead to the generation of large amounts of surface runoff, which is eventually conveyed into stormwater collection systems. Most of the time this leads to the rapid filling of closed conduits, such as sewers, in a highly unsteady fashion that can lead to the entrapment of large air pockets [Li and McCorquodale, 1999, Zhou et al., 2002, Vasconcelos and Wright, 2006]. Issues that have been linked to the presence of air in stormwater systems include increased pressure surges, loss of storage capacity, and geysering. Such issues have led to investigations aimed at the identification of interactions between entrapped air pockets within unsteady water flows.

There are at least three different types of studies linked to the behavior of entrapped air pockets. The first type approaches the problem of air pocket interactions in the perspective of stormwater systems in which air pockets are linked to flow regime transition episodes (either abrupt or gradual), and a major concern is the pressurization of air. The second type focuses on the removal of discrete air pockets in pipelines. Various formulas [Falvey, 1980, Pothof and Clemens, 2008, Pozos et al., 2010] have been proposed to predict the minimum average velocity to clear air pockets from pipelines based on air pocket dimension, pipeline slope, etc. The third type focuses on a relatively new research area and is discussed in this section. Instead of neglecting the air phase, the motion of air pockets in pipelines is accounted for in the flow regime transition episodes previously mentioned.

Studies focused on air pocket motion have dealt with fundamental flow aspects such as the advance of an air cavity or finite length air pocket from the open end of a pipe. The flow in such conditions can be considered as a type of non-Boussinesq flow and is created by density differences between two fluids. As explained earlier, Boussinesq currents occur when density differences between fluids are small, e.g. up to 2%. Non-Boussinesq currents occur when density differences are very large as in the spreading of an air pocket along the crown of a pipe partially filled with water. One of the earliest analytical investigations on gravity currents was conducted by [Benjamin, 1968]. Benjamin proposed a steady-state theory to

describe such air-cavity motion when air was allowed to flow freely into a tube initially filled with water. Benjamin determined the possible air cavity depths ($y/H \leq 0.5$ in which y is the depth of the air cavity and H is the height of the tube) and concluded that dissipation existed for depth ratios $y/H < 0.5$.

In an attempt to quantify the effects of surface tension and unsteadiness, which were not considered by Benjamin, [Wilkinson, 1982] conducted experiments in rectangular tubes filled with water in which one end was opened to admit air. One of the primary objectives was to describe the front speeds and shapes of the resulting air-cavities when the air inflow was throttled. In his experiments the energy-conserving, steady-state solution ($y/H = 0.5$) existed when the air was allowed to flow freely out of one end of the tube. Surface tension and wall boundary effects were negligible in such conditions. For throttled flows in which one end of the tube was partially opened, [Wilkinson, 1982] determined that the flow was unsteady when the depth ratio at the outlet was $0.22 \leq y/H < 0.5$. In this scenario the speed and shape of the air-cavity front was the same as for energy-conserving flows, but the front was followed by a hydraulic jump moving at a slower speed than the front. When the air-cavity depth ratio $y/H < 0.22$, the flow was again steady but corrections for surface tension were recommended. For this steady-state scenario, which was predominant for the experiments conducted in this work, [Wilkinson, 1982] obtained an analytical solution. One of the drawbacks of this approach is that the expression represents one equation for two unknowns: air pocket front velocity and depth.

[Baines et al., 1985] performed similar experiments except that a constant volume of air was released at one end of a rectangular tube. Three phases were observed in the experiments: the velocity and depth of the front were steady (phase 1); the front speed decreased monotonically in which there was a balance between inertia and drag (phase 2); the front erratically stopped and started before coming to rest (phase 3). The characteristics of phase 1 were generated a few tenths of a second after the initial gate release and are dependent on the initial depth ratio (y_0/H) where y_0 is the initial air pocket depth measured from the

pipe centerline. For ($0.7 \leq y_0/H \leq 1$), the flow resembled Benjamin's energy conserving theory. A different steady-state front was observed by the authors for smaller depth ratios in which the flow upstream of the nose resembled a "shallow neck". In both instances a shock developed that, once reflected off of the end wall, eventually overtook the front. This instance generates the beginning of phase 2 (the kinematics of phase 2 are independent of the initial depth ratio). This feature was also demonstrated in Boussinesq gravity currents by [Rottman and Simpson, 1983].

There is an important knowledge gap that stands at this point, which is linked to the inability to account for both the spreading and the pressurization of air pockets during simulations of rapid filling events. A standing challenge in this task is the inability of Saint-Venant equations to represent flow conditions at the edge of air pockets where free surface flows are curved and pressures are non-hydrostatic. A new modeling formulation that avoids the limitations of the Saint-Venant equations is needed, and is presented in this work.

Chapter 2

Knowledge Gaps and Objectives

Two-phase gravity current (GC) flows are observed in a number of cases that include civil and environmental engineering applications. The objective of this work is to focus on physical and numerical modeling for: Boussinesq gravity currents in open-channels and non-Boussinesq gravity currents in closed conduits. Knowledge gaps identified in the Section 1 for each research case are listed below:

- The quantitative focus of most lock-exchange GC experiments has involved the density distribution and leading edge trajectory. For these lock-exchange experiments, internal GC velocity measurements have not been provided (e.g. using MicroADV devices) that could potentially help in calibrating numerical models and provide insight into entrainment and its effect on GC motion.

- [Peng and Lee, 2010] used the planar laser-induced fluoroescence (PLiF) flow visualization technique to analyze instabilities at the front of gravity currents. They concluded what other researches have observed that two dominant instabilities exist at GC leading edges: the Kelvin-Helmholtz instability that leads to billows moving upstream of the GC head and the convective instability, which results in lobes and clefts at the GC front. [Peng and Lee, 2010] found that the convective instability leads to another instability related to vortex breakdown. These instabilities govern GC mixing and entrainment mechanisms highlighting the limitations in shallow water equation (SWE) modeling. More detailed frontal instability and turbulent flow structure measurements are necessary to better understand these mixing mechanisms and how to incorporate such effects in SWE models.

- Incorporating entrainment in 1D SWE modeling has lately received more attention [Adduce et al., 2012]. Empirical approaches have been proposed, but a more unified method that accounts for a wide range of channel geometries, depth ratios, density differences, slopes, stratification, grain size distribution, etc. would benefit the fluid mechanics community.

- GC modeling using the SWE has focused on finite difference method (FDM) and method of characteristics (MOC) based numerical approaches [Ungarish, 2009]. When resolving flow discontinuities in the lock-exchange problem, the shock-tracking method has been the primary modeling choice. For complex flow problems modeled with SWE (e.g. gravity currents propagating into ambient crossflows with multiple wall reflections), shock-tracking methods can be cumbersome and difficult to implement. An open question is whether shock-capturing approaches based on the finite volume method (FVM) constitute a better alternative.

- [Dai, 2014] conducted non-Boussinesq GC experiments with different density ratios ($0.05 \leq \epsilon \leq 0.17$) while varying the bottom slope ($0^\circ \leq \theta \leq 9^\circ$). They noted that there is a gap in experimental data for larger slopes and larger density differences. As pointed out in [Lowe et al., 2005], density ratios as low as 0.61 can be obtained with sodium iodide, but high costs are involved in conducting such experiments.

- [Ungarish, 2011] and [Rotunno et al., 2011] developed two-layer SWE models for non-Boussinesq high-Reynolds-number gravity currents accounting for the upstream-moving flow discontinuity that develops after gate release for large fractional depth. Boussinesq GC theory was extended for SWE models in which Boussinesq flows are treated as a special case of non-Boussinesq gravity currents. A large range of numerical results was presented in [Ungarish, 2011] by varying density differences and fractional depth. The SWE models were tested with Navier-Stokes models in [Rotunno et al., 2011] and [Baines et al., 1985] experiments in [Ungarish, 2011] with generally good

agreement. Another gap for SWE models applied to non-Boussinesq gravity currents is related to the mathematical model in which an extension to conservative and divergent format has not been proposed. Thus, these non-Boussinesq type SWE models have not been tested with nonlinear numerical schemes.

- [Hallworth et al., 1998] investigated gravity currents with initial ambient flows moving with (coflows) and against (counterflows) the GC. They developed a two-layer SWE model to predict such GC motion, but they restricted their investigation to systems with small fractional depth (i.e. $\phi \leq 0.5$) in which flow discontinuities do not develop. [Hogg et al., 2005] expanded on their work focusing on density intrusion gravity currents in which there was a constant influx of denser fluid near the center of a rectangular tank. One of the difficulties in both investigations was quantifying mixing effects in the initial release where SWE theory is invalid.

  [Robinson et al., 2013] expanded on the work of [Hallworth et al., 1998] conducted GC experiments in systems with steady periodic wave flow instead of a constant ambient flow velocity. In [Robinson et al., 2013] experiments qualitative results were provided in terms of observed wave regimes; however, the quantitative relationship between these wave regimes and expected concentrations is not presented as mentioned by the authors. Also, the relationship between the profile of the GC head and shearing caused by ambient wave motion needs more analysis.

- [Goldman et al., 2014] compared the one-layer SWE model with 2-D Navier-Stokes simulations for gravity currents with linear stratification. Results were presented for different quantities of GC stratification, ambient stratification and fractional depth. The one-layer SWE model showed deficiencies for large fractional depth and cases where waves slowed propagation by interacted with the GC head. An extension to two-layer SWE theory was recommended to overcome one-layer deficiencies but has not been developed. In addition, [Goldman et al., 2014] acknowledged the limitations

in 2-D Navier-Stokes models particularly for resolving eddies at the GC head in which 3-D models are recommended.

- [Marino et al., 2005] performed lock-exchange GC experiments focusing on leading edge characteristics. They concluded that the Froude number used in self-similar analytical solutions and leading edge boundary conditions for SWE models is effectively calculated using the initial lock depth (h_0) in the initial constant velocity (i.e. slumping) stage. As the GC enters the self-similar stage where there is a balance between inertia and drag [Simpson, 1997], [Marino et al., 2005] recommends a length scale based on the maximum depth at the rear of the gravity current head instead of h_0. They noticed that this Froude-like number varies with the Reynolds number over the range of 400-4500. [Marino and Thomas, 2009] extended this leading edge analysis to cases with non-rectangular cross-sections for light and heavy gravity currents.

  Most SWE models for gravity current flows use h_0 as a length scale in Fr calculations at the leading edge for the slumping and self-similar flow stages. In the transition between these stages, the Fr changes as the initial conditions are no longer important in the self-similar stage. [Marino et al., 2005] states that there is no justification in using the same Fr formulation throughout the propagation as implemented in existing SWE models. More work is necessary for quantifying depth and velocity relationships at the GC leading edge accounting for both slumping and self-similar flow stages.

- [Ungarish, 2008] investigated energy balances for lock-exchange gravity currents focusing on the leading edge BC. A major contribution was using shallow water theory to analyze such energy balances where steady-state hydraulic theory had been used in previous investigations. It was concluded that energy dissipation for this time-dependent case resembled Benjamin's theory for steady-state gravity currents. Other methods that compare better to experiments are treated as ad-hoc solutions. Moreover, [Ungarish, 2008] found that the implementation of energy conserving boundary conditions

resulted in unrealistic results for lock-exchange flows. It was emphasized that the loss of kinetic energy at the GC leading edge may be converted to the vertical dimension for real systems. The quantitative effect of this transfer of energy was not resolved in [Ungarish, 2008] as it was out-of-scope for a 1-D two-layer analysis.

- Although front conditions that relate GC depth and velocity have received a lot of attention, the implementation of leading edge boundary condition (BC) solution strategies needs more analysis. Existing front BC methods are based on MOC, so BC implementation can change for different SWE models (e.g. one-layer and two-layer models). For different flow applications, it is difficult to determine which solution strategy is appropriate. One of the MOC approaches uses interpolation (i.e. Specified Time Intervals, STI), but errors associated with this limitation are unknown. Clear numerical guidelines and/or a comprehensive comparison for BC solution strategies would clearly benefit SWE models.

  In [Ungarish, 2011] and [Rotunno et al., 2011] non-Boussinesq SWE models, a Grid-of-characteristic (GOC) MOC BC was utilized at the GC leading edge. The implementation of this front BC is more complex for non-Boussinesq gravity currents than their Boussinesq counterpart [Ungarish, 2011]. BC alternatives, such as the STI approach, have not been tested for two-layer non-Boussinesq SWE models.

- Initial conditions leading to air pocket formation and motion in closed conduits are not well understood; thus, accurate numerical modeling is difficult.

- GC research for non-Boussinesq, air-water flows has focused on analytical methods and qualitative observations. Few research investigations have predicted air pocket motion due to several complexities that include geometry, pipeline slope, surface tension, geometric complexity and limited availability of field and laboratory data. In a large

number of hydraulic applications (e.g. stormwater system design and pipeline priming), a viable modeling alternative to predict air pocket motion would be beneficial for the design of such systems.

- Integral models have been applied in a large number Boussinesq GC applications [Huppert and Simpson, 1980, Thomas et al., 2004] but rarely in the case of non-Boussinesq flows. [Baines et al., 1985] simulated air-water gravity currents with an integral-type model (also referred to as a Box model), but to our knowledge box models have not been applied to hydraulic systems with circular conduits, sloped pipelines or background flow velocities.

Some of the knowledge gaps listed above are analyzed in this work for Boussinesq and non-Boussinesq GC flows. The primary objectives are listed below:

- To measure internal velocities in high-Reynolds-number, Boussinesq lock-exchange experiments using MicroADV probes in both fluid layers;
- To develop depth-averaged velocity hydrographs for validation of SWE models in lock-exchange applications;
- To develop a shock-capturing SWE model for Boussinesq, lock-exchange gravity currents that accurately simulates leading edge trajectories and flow discontinuities throughout slumping and self-similar flow stages;
- To compare nonlinear FVM numerical schemes to FDM approaches for GC flows;
- To develop a simple yet accurate alternative for the leading edge BC used in SWE models and to provide a systematic comparison for existing GC front BC methods focusing on ease of implementation, continuity errors and computational time;
- To develop a 2-D Reynolds-Averaged-Navier-Stokes (RANS) model in OpenFOAM to assess one-layer SWE models in fixed-volume, Boussinesq GC applications.

- To formulate an integral model for non-Boussinesq gravity currents that accurately predicts air pocket motion in closed conduits for a wide range of pipe diameters, air pocket volumes and flow velocities.

Chapter 3

Methodology

The Methodology covers three research phases in which the first phase focuses on an experimental and numerical investigation on lock-exchange gravity currents. Additional sections deal with numerical investigations of leading edge BC solution strategies and integral models formulated for non-Boussinesq systems, respectively. It approximately follows the sequence of four journal papers that were published as a result of this research. The overall scope and main contributions for each section are summarized below:

- Lock-exchange: Experiments were performed in a 9.14 m long rectangular channel using saltwater and freshwater. The GC front trajectory was tracked with a 30 FPS video camera for three different density differences. A new approach used in this work involved the development of two Micro Acoustic Doppler Velocimeter (MicroADV) devices sampling at 30 Hz in both fluid layers. To our knowledge, MicroADV probes had not been previously used in this lock-exchange scenario. The MicroADV probes were each placed at three different depths near the middle of the channel. Velocity hydrographs were developed for both fluid layers and transformed in depth-averaged velocity results for comparison with SWE models.

- SWE modeling: The one and two-layer SWE models are both presented with a focus on finite volume and shock capturing methods. In order to develop a numerical model to simulate the lock-exchange experiments, a two-layer SWE model was developed as presented in [Hatcher and Vasconcelos, 2013a]. A key contribution was adapting existing SWE models to simulate gravity currents with large depth ratios (e.g. lock-exchange problem) without the need for explicit tracking of shocks. The proposed

numerical model is the first of its kind amenable to the finite volume method (FVM) and solved with nonlinear numerical schemes. Finally, the two-layer SWE model was extended to account for gravity currents propagating into ambient crossflows.

- Alternatives for flow solution at the GC leading edge: A new BC was implemented at the GC leading edge for the aforementioned SWE models. Using the one-layer SWE, a systematic comparison was made between the proposed solution strategy and two alternatives based on MOC as presented in [Hatcher and Vasconcelos, 2014]. The advantages and disadvantages are provided for each method focusing on ease of implementation, computational efficiency and continuity errors. In addition, lock-exchange experiments conducted by [Marino et al., 2005] as well as two Reynolds-Averaged-Navier-Stokes (RANS) models developed in OpenFOAM ($k-\epsilon$ and $\overline{v^2}-f$) were used to analyze the validity of SWE models.

- Integral model approach to simulate air pocket motion: This section follows experiments conducted by [Chosie, 2013] in a 101.6 mm diameter pipeline. Instead of focusing on more complex modeling tools, the integral model approach was selected based on simple yet fairly accurate results. This numerical modeling approach is popular for Boussinesq gravity currents in rectangular open channels but has not gained as much momentum for non-Boussinesq currents propagating in closed conduits. In this work two integral models are formulated to simulate air pocket motion in closed conduits and tested for a wide range of air pocket volumes and background flow velocities.

3.1 Lock-exchange gravity current experiments

Lock-exchange experiments were conducted in a 9.14 m long rectangular channel in order to validate the two-layer SWE model (Eq. 3.5) and to better describe GC flows such as those in the Mobile Bay channel. Experimental studies related to gravity currents are prevalent, but none have analyzed the use of MicroADV devices in describing lock-exchange

GC flows. Although the leading edge trajectory is tracked with HD video cameras, the focus of this experimental work is on obtaining velocity hydrographs. Depth-averaged velocities were obtained from the MicroADV results and are analyzed in Section 4.1.2.

3.1.1 Physical model construction and measurement devices

The acrylic channel was constructed in four segments as the acrylic sheets are only 2.44 m in length. In each component a 15 cm wide sheet that represents the channel bottom was welded to two acrylic sheets (40.6 cm wide) that represent the channel sides. Therefore, the maximum depth that could be achieved in the channel is 40.6 cm. After the side pieces were welded on top of the bottom sheet, the effective channel width was 12.7 cm. A wooden gate (2 cm thick) with rubber ends was constructed to separate the two fluids, which initiated the GC flow upon removal.

Before the acrylic sheets were welded together, openings were drilled into the acrylic. Then the acrylic sheets were tightened together with metal screws in order to increase the welding adhesion and to provide structural support. In the front of the physical model on the outside of the tank, small acrylic pieces around 5 in long were used to connect the adjacent acrylic sheets (Fig. 3.1). On the inside of the tank, adhesive tape was placed between the acrylic segments with silicon caulking applied along the edges in order to obtain a strong waterproof seal. As a result, the entire channel formed a cohesive and waterproof unit.

In this analysis it was important to position the MicroADV probes as close to vertical as possible in order to accurately measure the velocity in the longitudinal direction. The probes were held in place with a wooden support, and adhesive tape was applied to hold them in the vertical direction. The wooden support contains a cantilever section that hangs over the channel so that the ADV probes could be placed in the center of the tank.

3.1.2 Experimental variables and range of variation

Experiments were performed in a 9.14 m long and 12.7 cm wide rectangular channel (see Fig. 3.2) with the following initial conditions: $x_0 = 76.2$ cm, $h_0 = 40.6$ cm and $L = 914.0$ cm. Three different density differences were used ($\epsilon = 1\%$, 2% and 3%). There was no initial ambient motion in the experiments; however, ambient motion was generated upon gate release. Instead of implementing a large range of parameters (e.g. x_0, h_0, $\Delta\rho$), the experimental contributions focus on the analysis of downward-facing MicroADV probes measuring velocities in both fluid layers. In 1%, 2% and 3% experiments, MicroADV devices were measuring velocities near the center of the channel and the middle of each fluid layer (see Fig. 3.2).

For 1% and 2% density differences, MicroADV devices were also adjusted to measure velocities at different depths within each fluid layer: $h^*_{ADV} = h_{ADV}/h_0 = 0.063$, 0.125 and

Figure 3.1: Different components of the construction for the acrylic channel.

0.188 for the lower ADV; and $h^*_{ADV} = 0.375, 0.625$ and 0.875 for the upper ADV. These velocity hydrographs display the variation of velocity with depth and allow for comparison with CFD models. Obtaining velocities for a range of depths resulted in depth-averaged velocity results, which are compared to the two-layer SWE model in Section 4.1.2.

It is convenient to display the parameters for lock-exchange GC flows in terms of dimensionless units. Moreover, distance is normalized by the initial current length (x_0), depth by the initial GC depth (h_0), velocity by the initial celerity ($\sqrt{g'h_0}$), etc., as seen in [Ungarish, 2009]. This procedure allows for a comparison of various initial conditions while verifying consistency of results. For the experiments conducted in this work, the initial conditions and some of the dimensionless results are presented in Table 3.1.

Table 3.1: Experimental initial conditions and results for each experiment. Values for u_{m} were determined from a digital camera tracking the GC front.

Run	x_0 $[m]$	h_0 $[m]$	ρ_1 $[kg\,m^{-3}]$	g' $[ms^{-2}]$	u_{m} $[ms^{-1}]$	Re_{m} $[-]$	Fr_{H} $[-]$
1	0.762	0.406	1010	0.107	0.098	19952	0.468
2	0.762	0.406	1020	0.202	0.135	27657	0.472
3	0.762	0.406	1028	0.277	0.158	32423	0.473

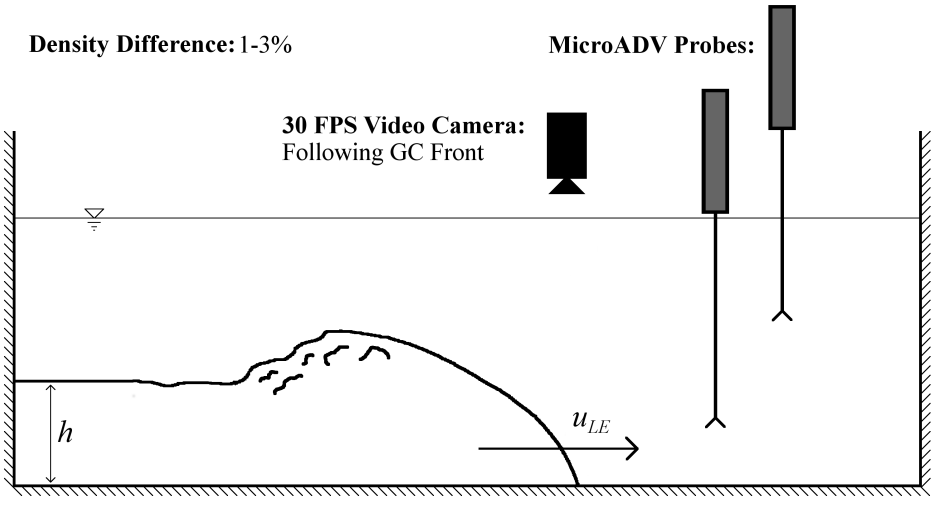

Figure 3.2: Schematic diagram of lock-exchange experiments (not to scale). The MicroADV probes were placed at three different depths within each fluid layer.

The mean Reynolds numbers in experiments ($Re_{\mathrm{m}} >> 1,000$) validated the inviscid assumption used later in this work for the SWE formulation. Because the initial depth was the same for each of the experiments, the total densimetric Froude number (Fr_{H}) should converge between each run conditions and indeed the results compared well to one another. Fr_{H} and Re_{m} were determined from the following expressions [Hacker et al., 1996], [Adduce et al., 2012]:

$$Fr_{\mathrm{H}} = \frac{u_{\mathrm{m}}}{\sqrt{h_0\, g'}} \qquad\qquad Re_{\mathrm{m}} = \frac{1}{2}\frac{u_{\mathrm{m}}\, h_0}{\nu} \tag{3.1}$$

The mean velocity of the GC (u_m) front was determined from high definition digital cameras tracking the front during the initial slumping stage (described in Section 3.1.3).

3.1.3 Experimental procedure and data analysis

Several experiments were conducted in a smaller scale tank ($x_0 = 20.3$ cm, $h_0 = 40.6$ cm and $L = 243.9$ cm) before official experiments in order to develop a consistent experimental program that involved the mixing procedure and the gate removal. Once consistent results for the GC trajectory were obtained in the smaller tanks, the experiments were performed in the 9.14 m tank that is presented in this work. Two duplicates were performed for each run to ensure that the results were consistent and properly obtained.

In this work salt was dissolved in one side of a rectangular channel to generate a predetermined density difference ($\Delta\rho$) between fluids. When dissolving the salt in water, it is imperative that the resulting density is accurately computed. Methods that have been implemented to determine the density are: salinity tables, polynomial equations, hydrometers and refractive index measurements. Because of simplicity and accuracy of results, the difference in density for this work was estimated from a polynomial expression in www.csgnetwork.com/h2odenscalc.html, which was provided by the University of Michigan and NOAA:

$$\rho = \rho_0 + Ac + Bc^{3/2} + 0.00048314c^2 \tag{3.2}$$

where

$$A = 0.824493 - 0.0040899\,T + 0.000076438\,T^2 - 0.00000082467\,T^3 + 0.0000000053675\,T^4$$

$$B = -0.005724 + 0.00010227\,T - 0.0000016546\,T^2$$

$$\rho_0 = 1000\,\frac{1 - (T + 288.9414)}{508929.2(T + 68.12963)} * (T - 3.9863)^2$$

in which A and B are polynomial parameters, ρ is the density of the denser fluid in $kg\,m^{-3}$, T is the temperature in $^{\circ}C$ and c is the salt concentration in mg l^{-1}. The initial salt concentration was determined from this relationship, and the resulting density difference was re-evaluated using precision hydrometers. These hydrometers provided the density with an error of approximately 5% or less. In addition to accurate data measurement, experiments were performed relatively quickly.

For the velocity hydrograph measurements, two MicroADV probes sampling at 20 Hz were placed near the middle of the tank in order to determine the velocities for the denser current and ambient fluid. The MicroADV devices were placed at $x* = 7.68$ and $x* = 7.70$ for the lower and upper ADV, respectively. Although three-dimensional velocities were obtainable, the focus of the data analysis was on the longitudinal velocities. The lower ADV probe was placed 10.2 cm from the channel bottom, and the upper probe was placed 33.0 cm from the channel bottom in order to measure the ambient velocities. As mentioned in Section 3.1.2, ADV depths were adjusted for 1% and 2% experiments to develop depth-averaged results. The data was recorded at 20 Hz for about 250 s or when the GC front reflected back and forth twice.

The trajectory of the front was also tracked with a 1080p high-definition digital camera moving with the GC front and recording at 30 frames per second. The cameras were positioned at the leading edge normal to the channel sides, and measurements were made at 10 cm intervals. The experimental errors were within acceptable limits ($\Delta x^* = 0.03$ and $\Delta t^* = 0.01$).

3.2 Shallow water equation modeling

There are three primary cases related to 1-D SWE modeling that are highlighted all with the following model objectives: focus on computationally efficient solutions, minimize continuity errors and employ shock-capturing methods amenable to FVM schemes. Each case correlates to a unique SWE formulation: one-layer, two-layer and two-layer accounting for ambient crossflows. Unlike previous related work, each mathematical model presented here is written in conservative and divergent format and solved with both linear and nonlinear FVM schemes. The SWE models are written in such a way that the conserved variables ($\vec{\mathbf{U}}$) and fluxes ($\mathbf{F}(\vec{\mathbf{U}})$) are equivalent. This methodology allows the LHS of the momentum equations to be solved using the same procedure/numerical scheme, while the model differences are mathematically expressed in the source terms ($\mathbf{S}(\vec{\mathbf{U}})$).

3.2.1 One-layer shallow water equations

One of the contributions of this work is related to the front BC solution strategies (Section 3.3) incorporated in SWE models, which was recently accepted in the IAHR Journal of Hydraulic Research. To compare these leading edge boundary conditions, the one-layer SWE is utilized as presented in [Ungarish, 2007]. This numerical model is ideal for smaller depth ratios in which the one and two-layer SWE models are indistinguishable [Ungarish, 2009]. For the lock-exchange problem ($\phi = 1$) analyzed subsequently in this work, depth gradients are much larger and the two-layer SWE are recommended.

The one-layer SWE model is implemented in this work for constant-volume and density intrusion gravity currents with $\phi \leq 0.5$. This one-layer model is written below in conservative

and divergent format amenable for solving with nonlinear Riemann solvers:

$$\frac{\partial \vec{\mathbf{U}}}{\partial t} + \frac{\partial \mathbf{F}(\vec{\mathbf{U}})}{\partial x} = \mathbf{S}(\vec{\mathbf{U}})$$

$$\vec{\mathbf{U}} = \begin{bmatrix} h \\ \\ uh \end{bmatrix} \qquad \mathbf{F}(\vec{\mathbf{U}}) = \begin{bmatrix} uh \\ \\ \dfrac{(uh)^2}{h} + \dfrac{1}{2}g'h^2 \end{bmatrix} \qquad \mathbf{S}(\vec{\mathbf{U}}) = \begin{bmatrix} 0 \\ \\ 0 \end{bmatrix} \tag{3.3}$$

in which h and u are the depth and velocity of the GC, respectively. Unlike in previous works, the SWE models are solved with the FVM method in which interface fluxes are computed to determine center-cell values of h and uh. The following expression performs the updates on the conserved variables for each computational cell i at the time step $n+1$:

$$\vec{\mathbf{U}}_i^{n+1} = \vec{\mathbf{U}}_i^{n} + \frac{\Delta t}{\Delta x}\left(\mathbf{F}(\vec{\mathbf{U}})_{i-1/2}^{n+1/2} - \mathbf{F}(\vec{\mathbf{U}})_{i+1/2}^{n+1/2}\right) + \mathbf{S}(\vec{\mathbf{U}})\Delta t \tag{3.4}$$

where $\mathbf{F}(\vec{\mathbf{U}})_{i\pm1/2}^{n+1/2}$ are the interfacial fluxes, which are calculated with various numerical schemes. Unless otherwise noted, the nonlinear HLL Riemann solver [Toro, 2001] is used in this work. To the author's knowledge, the one-layer SWE applied to gravity currents has not been previously written in divergent format or solved with nonlinear schemes.

One may notice the similarities between this mathematical model and the traditional SWE used to solve dam break flows. The primary difference lies in the gravitational acceleration term where gravity (g) is replaced by the reduced gravity (g') [Ungarish, 2009]. This change in $\mathbf{F}(\vec{\mathbf{U}})$ accounts for buoyancy effects in a Boussinesq system. When water and air are the two fluids under consideration, $g' \approx g$, and Eq. 3.3 reduces to the traditional SWE. One can also formulate Eq. 3.3 from the two-layer SWE Eq. 3.5 by eliminating the two-layer source terms. As subsequently stated, this one-layer SWE model is used in Section 3.3 to compare front boundary conditions for constant-volume and density intrusion gravity currents.

3.2.2 Two-layer shallow water equations

To predict GC motion in lock-exchange experiments outlined in Section 3.1, a two-layer SWE model was proposed. In one-layer implementations of the SWE, influences of the ambient fluid are neglected except in the reduced gravity. However, when the fractional depth ϕ approaches unity as in the lock-exchange experiments conducted for this work, the ambient velocity becomes an important parameter. This potential problem led to the mathematical model of the two-layer shallow water equations used for Boussinesq gravity currents as formulated by [Rottman and Simpson, 1983]. This formulation reduced the two-layer SWE from four partial differential equations (PDEs) to two. The upper layer continuity equation was omitted, and the two momentum equations were combined. Because their model was unable to simulate shocks, a new two-layer SWE model was formulated that tracks these sharp gradients with a shock capturing approach. This Section is based on the recent publication in the Journal of Hydraulic Engineering [Hatcher and Vasconcelos, 2013a] where the two-layer SWE model was used to simulate lock-exchange experiments that are presented in this work.

As in the one-layer SWE amenable to nonlinear FVM scheme, the two-layer SWE is written below in conservative and divergent format:

$$\frac{\partial \vec{\mathbf{U}}}{\partial t} + \frac{\partial \mathbf{F}(\vec{\mathbf{U}})}{\partial x} = \mathbf{S}(\vec{\mathbf{U}})$$

$$\vec{\mathbf{U}} = \begin{bmatrix} h \\ uh \end{bmatrix} \qquad \mathbf{F}(\vec{\mathbf{U}}) = \begin{bmatrix} uh \\ \dfrac{(uh)^2}{h} + \dfrac{1}{2} g' h^2 \end{bmatrix} \qquad \mathbf{S}(\vec{\mathbf{U}}) = \begin{bmatrix} 0 \\ Ah^2 \dfrac{\partial u}{\partial x} + Bg'h \dfrac{\partial h}{\partial x} \end{bmatrix} \tag{3.5}$$

$$A = \frac{2\,u}{H-h} \qquad B = \frac{h/H\,(1-h/H)^2 + \left(u/\sqrt{g'H}\right)^2}{(1-h/H)^2}$$

in which the upper layer parameters were substituted out of the momentum equation as in [Rottman and Simpson, 1983]. The transition to divergent format involved some algebraic

manipulation and the substitution of the continuity equation back into the linear momentum equation for the denser current layer.

In Eq. 3.5 A and B are components of the source terms presented by [Rottman and Simpson, 1983] rewritten to highlight the potential problems as $h \to H$. When the depth ratio approaches unity, it is clear that the solution of both terms approaches a zero divided by zero solution in which instabilities emerge (the GC velocity (u) approaches zero in such conditions because of the horizontal free surface). The proposed solution in Eq. 3.5 separates the depth and velocity gradient components of the source term because their effect on stability and shock simulation is different. For the depth gradient component of the source term, there is a relatively simple solution in that $B = 1$ when $h = H$. This value for B was enforced by [Klemp et al., 1994] and [Ungarish and Zemach, 2005] as a constraint to ensure the front velocity did not exceed the characteristic velocity. However, the numerical solution may become unstable primarily because of the velocity gradient component of the source term, which is multiplied by A. To overcome this problem, a term ($\epsilon_h H$) with small magnitude was added to the denominator of A to ensure that the solution could not become undefined. As a result, this work implements the following expression for A:

$$A = \frac{2uh^2}{(1+\epsilon_h)H - h} \tag{3.6}$$

The value of the parameter ($\epsilon_h = 0.01$) was selected on the basis of stability and accuracy of simulation. Albeit pragmatic, results show that the addition of 1% of H in the denominator of the variable A managed to stabilize the solution and yield accurate predictions for GC flows.

The advantage of the proposed mathematical model is simplicity in which regions with steep gradients are accounted for without resorting to explicit numerical tracking. This procedure enables the same numerical scheme to be applied everywhere in the solution domain except of course at the boundary conditions (upstream wall and GC leading edge).

It is later shown that the proposed shock-capturing method compares well to the shock-tracking approach implemented by [Klemp et al., 1994] and [Ungarish and Zemach, 2005], specifically at describing the interface between the two fluids. The novelty in the proposed SWE model is highlighted in the ability to resolve shocks without the use of explicit tracking. In the lock-exchange problem, a backward moving shock is developed upon gate release and another shock is developed after the first is reflected off of a physical boundary. To the authors' knowledge, this two-layer SWE solution for lock-exchange GC is the first of its kind to incorporate non-linear approximate Riemann solvers (e.g. HLL scheme) within a finite volume framework, which has been proven to yield accurate predictions for sharp fronts in free-surface flow modeling, as illustrated in many previous works such as [Toro, 2001, Macchione and Morelli, 2003].

3.2.3 Two-layer shallow water equations accounting for ambient crossflows

Oftentimes, these gravity currents contain ambient crossflows, which are not accounted for in the previous two-layer SWE formulation. This limitation motivated the formulation of another numerical model presented in a recent ASCE-EWRI conference paper [Hatcher and Vasconcelos, 2013b] that is able to simulate lock-exchange GC flows with moving ambients. The primary difference in the new formulation is related to the control volume approach that was used to eliminate the ambient velocity (u_2) from the momentum equation. In the presence of ambient crossflows, this expression is $u_1 h_1 + u_2 h_2 = UH$ where U is the ambient velocity and the subscripts 1 and 2 represent the current and ambient fluid layers, respectively. Incorporating this control volume approach into the two-layer SWE formulation, the updated mathematical model is presented below for the lower GC layer with the subscripts

removed:

$$\frac{\partial \vec{\mathbf{U}}}{\partial t} + \frac{\partial \mathbf{F}(\vec{\mathbf{U}})}{\partial x} = \mathbf{S}(\vec{\mathbf{U}})$$

$$\vec{\mathbf{U}} = \begin{bmatrix} h \\ uh \end{bmatrix} \qquad \mathbf{F}(\vec{\mathbf{U}}) = \begin{bmatrix} uh \\ \dfrac{(uh)^2}{h} + \dfrac{1}{2}g'h^2 \end{bmatrix} \qquad \mathbf{S}(\vec{\mathbf{U}}) = \begin{bmatrix} 0 \\ Ah^2\dfrac{\partial u}{\partial x} + Bg'h\dfrac{\partial h}{\partial x} \end{bmatrix} \tag{3.7}$$

$$A = \frac{u}{H} + \frac{uh + uH - 2UH}{H(H-h)} \qquad B = \frac{h}{H} + \frac{u^2 + U^2 - 2uU}{g'H(H-h)^2}$$

in which $\vec{\mathbf{U}}$ and $\mathbf{F}(\vec{\mathbf{U}})$ are the same as in Eq. 3.5, but $\mathbf{S}(\vec{\mathbf{U}})$ is updated to incorporate the ambient velocity. The source terms appear equivalent for both two-layer models, but changes are present in the source term parameters A and B. The similarity between mathematical models allows for the same solution procedure using nonlinear Riemann solvers.

3.2.4 Numerical implementation of shock-capturing shallow water equation models

The SWE models are tested for both constant-volume and constant-flux (density intrusion) GC flows. The numerical implementation for the aforementioned GC problems is highlighted including boundary conditions and initial conditions. The differences between GC flows with and without ambient crossflows are also discussed. One of the most heavily studied components of the numerical implementation for GC SWE models is the front condition. This condition is briefly discussed since it is a key component of leading edge BC solutions, which is the focus of Section 3.3. As previously stated, the HLL numerical scheme [Toro, 2001] is utilized unless other stated.

Constant-volume gravity currents

The constant-volume scenario is broken up into two problem types: the lock-exchange problem [Rottman and Simpson, 1983] and partial depth release problem with ambient crossflows [Hallworth et al., 1998]. In the lock-exchange case, denser fluid is released at one

end of a long channel containing lighter fluid. The fluids are typically set in motion by the removal of a gate that separates both fluids in which density differences drive the flow. The two-layer SWE model (Eq. 3.5) is compared to this GC scenario since sharp gradients/shocks are expected to occur upon gate release.

For the lock-exchange problem, the initial conditions are simple: $u = 0$, $h = H$ for $x \leq x_0$ and $h = 0$ for $x > x_0$. There are two types of boundary conditions located at either the GC leading edge or at physical walls. The solution alternatives at physical walls are straightforward and consistent for each GC flow scenario. Enforce zero flow ($u = 0$) along with a relevant characteristic equation or apply a reflective BC with the aid of a virtual cell, as presented in [Toro, 2001]. In this work the MOC is used at wall boundary conditions, and the DC approach is used at the GC leading edge (see Section 3.3.3).

For the ambient crossflow case, the partial depth ($\phi < 1$) release occurs near the center reach of the channel (see Fig. 3.3a). The boundary conditions for this constant-volume problem are slightly different than traditional lock-exchange simulations. Because the denser fluid is released near the center of the channel, GC fronts spread in both directions horizontally, so two leading edge boundary conditions are implemented as described in [Hallworth et al., 1998]. The following expressions represent the front conditions for the left and right GC leading edge, respectively:

$$u = -Fr\sqrt{g'h} + U \qquad\qquad u = Fr\sqrt{g'h} + U \tag{3.8}$$

in which the ambient velocity (U) is known and can be positive or negative. The Froude number at the GC leading edge (Fr) was computed from the HS expression [Huppert and Simpson, 1980], as presented in [Hallworth et al., 1998]. The leading edge BC, which utilizes this front condition, follows the DC approach [Hatcher and Vasconcelos, 2013a] and is highlighted in Section 3.3.3. For the traditional lock-exchange problem [Rottman and Simpson, 1983], only the second expression in Eq. 3.8 is utilized as discussed in Section 3.3.

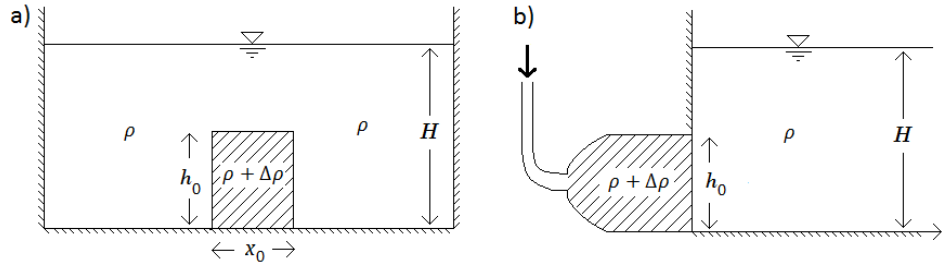

Figure 3.3: Schematic diagram of GC flows with ambient crossflows. a) constant-volume GC and b) density intrusion GC.

Lastly, in their experiments [Hallworth et al., 1998] were unable to insert the denser fluid into the center of the tank without dilution and momentum effects caused by a moving ambient flow. The model presented in this work is compared to [Hallworth et al., 1998] idealized two-layer SWE model in which the aforementioned mixing effects were neglected. The comparison is for smaller depth ratios ($\phi = 0.25$) since their model is unable to simulate shocks.

Density intrusion gravity currents

For the constant-flux simulations, denser fluid was flowing horizontally into a channel with constant velocity (see Fig. 3.3b). The ambient fluid was either moving with the current (coflow), moving against the current (counterflow) or stagnant. [Hatcher and Vasconcelos, 2014] analyzed the one-layer SWE for density intrusion gravity currents in stagnant flow conditions mimicking experimental conditions by [Wright and Paez-Rivadeneira, 1996]. As in the constant-volume simulations, the DC front condition was used at the GC front unless otherwise noted. The inlet dimensions (specifically h_{in}) and fluid densities were constant throughout the simulation. h_{in} and u_{in} were enforced at the upstream physical BC.

Enforcing both conserved variables in SWE simulations may result in numerical errors. In this case the errors were expressed in terms of continuity errors defined by the difference between initial and final GC volumes, which increased when inlet conditions were enforced (less than 1% difference). Although these continuity errors may be negligible depending on

the modeling objectives, an alternative solution alleviated this problem in a few trial runs (u_{in} was enforced and h_{in} was computed with a characteristic equation). However, h_{in} was enforced in this work to match with [Paez-Rivadeneira, 1997] experimental conditions.

[Paez-Rivadeneira, 1997] performed dozens of experiments with and without ambient crossflows, which were moving with (coflows) or against (counterflows) the GC. These experiments were used for comparison against the SWE model. The initial conditions for this model are slightly different than in [Paez-Rivadeneira, 1997] experiments. Instead of freshwater (i.e. the lighter ambient fluid) initially occupying the entire solution domain, the simulation begins with a small number of cells that contain denser fluid (see [Bonnecaze et al., 1995]). These saltwater cells were required for model stability but have a minor effect on the GC propagation.

3.3 Alternatives for flow solution at the GC leading edge

As mentioned in Section 1.4, front BC solution strategies are required for GC models using the SWE. The three leading edge BC alternatives are analyzed in detail in the following subsections. The success of each approach is determined based on computational efficiency and continuity errors in addition to ease of implementation as explained in [Hatcher and Vasconcelos, 2014]. The most popular approach (GOC) has been implemented in [Rottman and Simpson, 1983], [Ungarish, 2007], etc. and is further discussed in 3.3.1. The STI approach was implemented in [Hallworth et al., 1998], but the details were not covered and further explanation is necessary. After the MOC approaches are covered, the newly proposed DC method is presented in Section 3.3.3. The details of the formulations and implementations are highlighted following the recent publication [Hatcher and Vasconcelos, 2014].

3.3.1 Grid-of-Characteristics (GOC) approach

The GOC approach has the simplest concept of all the methods. It involves the combination of a front condition and a $C+$ characteristic equation that is tracked within a

characteristic line originated at a system boundary. This provides two equations that allow for the solution of the two unknowns $[h_{LE}, uh_{LE}]^T$ at the GC leading edge cell (LE subscript). When the model requires the solution at specified intervals, one method to implement the GOC approach is to generate the characteristic lines at every time step (e.g. at a physical boundary) and to track them so that the corresponding characteristic equation can be used in the BC computation (see Fig. 3.4). This is an important distinction from the STI method, which generates these characteristic lines at the vicinity of the GC leading edge. While the continuous generation and tracking of characteristic lines is computationally costly, particularly for finer grids, the GOC method benefits from no loss of accuracy caused by interpolation that is required in the STI method.

For constant-volume gravity currents, the depth varies over time at the upstream wall (cell 1), but the velocity is always zero. Tracking the characteristic lines over time brings the Riemann invariant values ($u+2c$) from the wall to the leading edge of the GC. The resulting

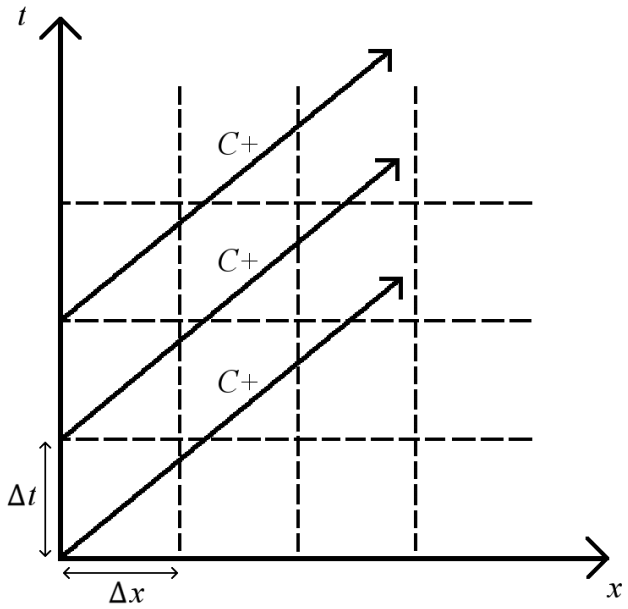

Figure 3.4: Diagram of the GOC approach, where $C+$ characteristic lines (not to scale and can be nonlinear) are generated at each time step at the upstream boundary. These travel towards and eventually reach the GC leading edge.

set of equations is thus:

$$u_{\text{cell:1}} + 2\sqrt{g'h_{\text{cell:1}}} = u_{\text{LE}} + 2\sqrt{g'h_{\text{LE}}} \tag{3.9a}$$

$$u_{\text{LE}} = Fr_{\text{LE}}\sqrt{g'h_{\text{LE}}} \tag{3.9b}$$

in which $u_{cell:1}$ is 0 at the upstream physical boundary, and $h_{cell:1}$ is the depth at the wall that was observed when the characteristic line was generated, at an earlier time step. The value of $h_{cell:1}$ will be constant and equal to the initial depth h_0 until the depression wave generated by the initial gate release arrives at the wall (for constant volume simulations). Up to that moment in the simulation, flow conditions are consistent with a simple wave condition [Sturm, 2010] and there is no need to generate/track characteristic lines. As the flow depth drops at the wall, characteristic lines are created each time step and the trajectory of this line is updated during the simulation using the $C+$ characteristic equation ($dx/dt = u + c$) evaluated with the local flow conditions between the wall and the leading edge of the GC. Once a new characteristic line reaches the GC front, Eqs. 3.9a and 3.9b are solved iteratively for h_{LE} and u_{LE}. The position of the front advance (x_{LE}^{n+1}) is updated according to the kinematic condition:

$$\Delta x_{\text{LE}}^{\text{n+1}} = \Delta x_{\text{LE}}^{\text{n}} + \Delta t \cdot u_{\text{LE}} \tag{3.10}$$

Once Δx_{LE}^{n+1} equals the internal cell length (Δx), one more computational cell of length Δx is added to the solution domain and Δx_{LE}^{n+1} and Δx_{LE}^{n} are reduced by Δx. In the case of density intrusion gravity currents tested in this work, both $h_{cell:1}$ and $u_{cell:1}$ are predefined by the problem conditions. Unlike constant-volume gravity currents, density intrusion problems involve non-zero velocity conditions at the upstream boundary. Since $h_{cell:1}$ and $u_{cell:1}$ (and respective Riemann Invariants) are constant throughout the problem, there would be no need to track the characteristic lines. However, this tracking is performed to consistently quantify the computation effort between the three tested approaches.

3.3.2 Specified Time Intervals (STI) approach

The STI approach, similarly to GOC, also utilizes the MOC. However, instead of tracking characteristic lines in the space-time grid from the line origin, interpolation between neighbor computational cells is utilized. It thus allows the calculation of the relevant Riemann invariant used in the computation of flow conditions along with the front condition much more rapidly decreasing computational effort. The approach is consistent with traditional implementation of the MOC-Hartree method at boundary conditions [Sturm, 2010] except that the location of the BC is updated with time. Using Fig. 3.5 as reference, integration of the $C+$ characteristic equation and the corresponding trajectory of the characteristic line yields:

$$u_{\mathrm{P}} - u_{\mathrm{R}} + (g'/c_{\mathrm{R}})\,(h_{\mathrm{P}} - h_{\mathrm{R}}) \tag{3.11}$$

$$x_{\mathrm{P}} - x_{\mathrm{R}} = (u_{\mathrm{R}} + c_{\mathrm{R}})\,\Delta t \tag{3.12}$$

The subscript P corresponds to a point immediately upstream of the leading edge in the next time step where the flow solution (u_P, h_P) at the leading edge is obtained. Point R is the origin of the $C+$ characteristic line that arrives at point P, bringing the information on the Riemann invariants (Eq. 3.11) to be applied in the solution of the flow in the BC. It is assumed that flow conditions at point P correspond to the conditions at the leading edge, less than Δx away. This approach is tested with good accuracy in comparison with the other front BC approaches with time steps ranging from 2 ms to 1 s (see Section 4.2.1).

While conditions at points A and B (previous time step) are known, flow depth, velocity, and celerity at point R are unknown, and this is where interpolation is introduced. A potential drawback of STI interpolation is the generation of inaccuracies in the solution, especially in locations where there are strong gradients. Assuming that the previous time step index is denoted by n, the computation of u_R, c_R and h_R follows the expressions presented

in [Sturm, 2010]:

$$u_{\mathrm{R}} = \frac{u_{\mathrm{B}}^{\mathrm{n}} + r\left(-u_{\mathrm{B}}^{\mathrm{n}} c_{\mathrm{A}}^{\mathrm{n}} + u_{\mathrm{A}}^{\mathrm{n}} c_{\mathrm{B}}^{\mathrm{n}}\right)}{1 + r\left(u_{\mathrm{B}}^{\mathrm{n}} - u_{\mathrm{A}}^{\mathrm{n}} + c_{\mathrm{B}}^{\mathrm{n}} - c_{\mathrm{A}}^{\mathrm{n}}\right)} \tag{3.13a}$$

$$c_{\mathrm{R}} = \frac{c_{\mathrm{B}}^{\mathrm{n}} + r u_{\mathrm{R}}\left(c_{\mathrm{A}}^{\mathrm{n}} - c_{\mathrm{B}}^{\mathrm{n}}\right)}{1 + r\left(c_{\mathrm{B}}^{\mathrm{n}} - c_{\mathrm{A}}^{\mathrm{n}}\right)} \tag{3.13b}$$

$$h_{\mathrm{R}} = h_{\mathrm{B}}^{\mathrm{n}} - r\left(h_{\mathrm{B}}^{\mathrm{n}} - h_{\mathrm{A}}^{\mathrm{n}}\right)\left(u_{\mathrm{R}} + c_{\mathrm{R}}\right) \tag{3.13c}$$

Once the parameters in Eqs. 3.13a-3.13c have been computed, Eq. 3.11 is solved alongside a front condition to determine $u_P = u_{LE}$ and $h_P = h_{LE}$. The update of the GC leading edge location uses the same kinematic condition that was presented for the GOC front BC (Eq. 3.10).

3.3.3 Dual-Cell (DC) approach

As pointed out, despite the relative simplicity behind MOC-based methods to provide closure to the flow calculation at the leading edge of gravity currents, both GOC and STI approaches have limitations. The GOC approach promotes explicit tracking of characteristic

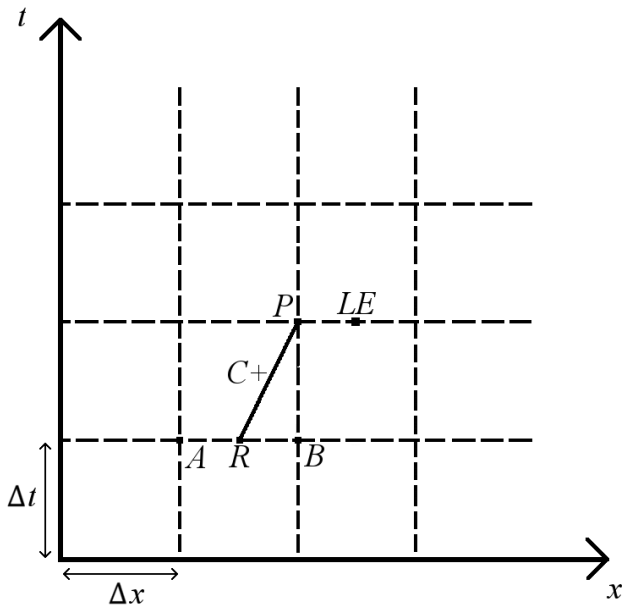

Figure 3.5: The numerical solution for the STI method in which the characteristic grid is superimposed onto a rectangular grid for a single time step. Adapted from [Sturm, 2010].

lines that may become computationally intensive in some cases. On the other hand, the STI approach involves interpolation that may impact model accuracy. In addition, characteristic equations for two-layered flows [Rottman and Simpson, 1983] are significantly more complex and difficult to implement.

These combined factors led to the development of an alternative method [Hatcher and Vasconcelos, 2013a] that does not depend on characteristic equations, but rather on flow conditions at two computational cells located at the leading edge region of the flow. This approach, referred to as Dual-Cell (DC) method, can be applied to one and two-layer GC flows without alterations. Like MOC-based approaches, it also requires a front condition to achieve flow closure at the leading edge of the GC. The DC method combines the enforcement of continuity, linear momentum, and the kinematic condition at the GC leading edge assuming that the front spans over two cells: (1) cell LE corresponds to a computational cell fully occupied by the dense fluid and (2) cell $LE + 1$ undergoes the advance of the current and is not yet completely filled (see Fig. 3.6 for reference).

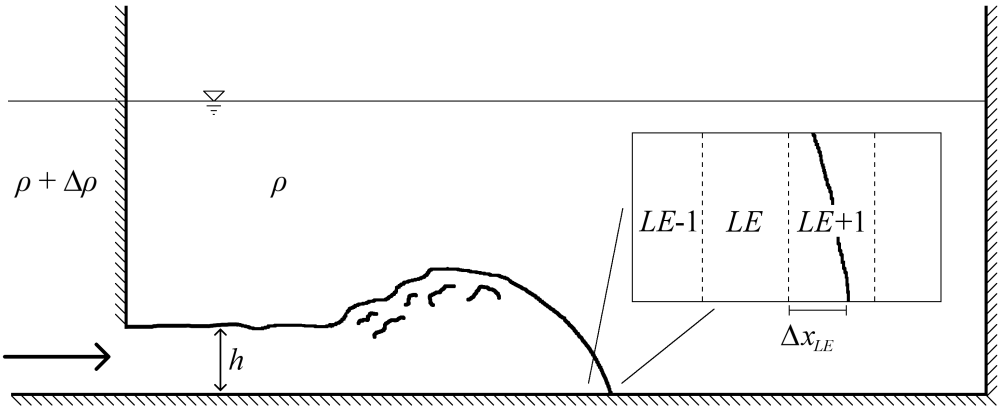

Figure 3.6: Schematic diagram of the DC approach implemented for density intrusion gravity currents with two cells representing the leading edge: LE and $LE + 1$.

The continuity equations utilized at the leading edge BC cells are presented below:

$$Continuity \begin{cases} \dfrac{dA_{\text{LE}}}{dt} = \Delta x \dfrac{dh_{\text{LE}}}{dt} = uh_{\text{ LE-1}} - uh_{\text{ LE+1}} & \text{(cell: LE)} \\ \dfrac{dA_{\text{LE+1}}}{dt} = \dfrac{d(\Delta x_{\text{ LE+1}}\, h_{\text{LE+1}})}{dt} = uh_{\text{ LE}} & \text{(cell: LE+1)} \end{cases} \tag{3.14}$$

in which A is the cell area: $A = \Delta x\, h_{\text{LE}}$ for cell LE and $A = \Delta x_{\text{LE+1}} h_{\text{LE+1}}$ for cell LE+1. The continuity equation is slightly more complex for cell LE+1 because both the depth $h_{\text{LE+1}}$ and the cell length $\Delta x_{\text{LE+1}}$ change with time as indicated in Fig. 3.6. The following expression represents the x-momentum equation that is implemented at the leading edge cell (LE):

$$\sum F_x = \sum_{cs} \dot{m}_{\text{LE+1}} u_{\text{LE+1}} - \sum_{cs} \dot{m}_{\text{LE}} u_{\text{LE}} \tag{3.15}$$

where $\dot{m} = \rho_c\, uh$ is the mass flow rate. The set of momentum and continuity equations along with the front condition and the kinematic condition used in the DC method is presented below:

$$DC \begin{cases} \big[\text{I}\big] & \rho_c \cdot uh^{\,\text{n+1}}_{\text{LE}} \Big(\dfrac{uh^{\,\text{n+1}}_{\text{LE+1}}}{h^{\,\text{n+1}}_{\text{LE}}} - \dfrac{uh^{\,\text{n+1}}_{\text{LE-1}}}{h^{\,\text{n+1}}_{\text{LE}}} \Big) + F_{\,2} - F_1 = 0 \\ \big[\text{II}\big] & h^{\,\text{n+1}}_{\text{LE}} = h^{\,n}_{\text{LE}} + \dfrac{\Delta t}{\Delta x} (uh^{\,\text{n+1}}_{\text{LE-1}} - uh^{\,\text{n+1}}_{\text{LE+1}}) \\ \big[\text{III}\big] & uh^{\,\text{n+1}}_{\text{LE+1}} = h^{\,\text{n+1}}_{\text{LE+1}} \sqrt{g' h^{\,\text{n+1}}_{\text{LE+1}}}\, Fr_{\text{LE+1}} \\ \big[\text{IV}\big] & \Delta x^{\,\text{n+1}}_{\text{LE+1}} = \Delta x^{\text{n}}_{\text{LE+1}} + \Delta t \dfrac{uh^{\,\text{n+1}}_{\text{LE+1}}}{h^{\,\text{n+1}}_{\text{LE+1}}} \\ \big[\text{V}\big] & uh^{\,\text{n+1}}_{\text{LE}} = \dfrac{1}{\Delta t} \Big[\Delta x^{\,\text{n+1}}_{\text{LE+1}} (h^{\,\text{n+1}}_{\text{LE+1}} - h^{\,\text{n}}_{\text{LE+1}}) + h^{\,\text{n+1}}_{\text{LE+1}} \big(\Delta x^{\,\text{n+1}}_{\text{LE+1}} - \Delta x^{\,\text{n}}_{\text{LE+1}} \big) \Big] \end{cases} \tag{3.16}$$

where n is the time step index, F_1 is the upstream hydrostatic force at the interface between cells LE-1 and LE, and F_2 is the downstream hydrostatic force at the interface between cells LE and LE+1. These five equations represent: 3.16$\big[\text{I}\big]$ the linear momentum balance at cell LE; 3.16$\big[\text{II}\big]$ the local continuity at cell LE; 3.16$\big[\text{III}\big]$ the enforcement of a front condition relating

depth and velocity at cell LE+1; 3.16[IV] the kinematic condition, which updates the front position $\Delta x_{\mathrm{LE+1}}^{\mathrm{n+1}}$, at cell LE+1; and 3.16[V] the local continuity at cell LE+1.

These equations are solved iteratively for the pair of cells at the edge of the computational domain until the advance of the GC front at cell LE+1 (i.e $\Delta x_{\mathrm{LE+1}}^{\mathrm{n+1}}$, given by $\sum u_{\mathrm{LE+1}} \Delta t$) exceeds the cell size Δx. When this occurs, the front of the GC enters a new cell and $\Delta x_{\mathrm{LE+1}}^{\mathrm{n+1}}$ is reset to zero and the process starts again for the set of the two new leading edge cells.

As the result section shows, this alternative to compute the boundary conditions is shown to be accurate for one and two-layer SWE models, comparing well with experimental data collected in this work as well as with previous investigations. For one-layer gravity currents using the DC method, results are compared with 2D RANS simulations.

3.4 Laterally-averaged RANS modeling of Boussinesq gravity currents

The other main component of the work included in [Hatcher and Vasconcelos, 2014] focuses on the validity of SWE models or in this case, the one-layer SWE model. One form of validation is based on lock-exchange experiments conducted by [Marino et al., 2005]. The other method for validation, which is the focus of this section, is RANS modeling that was developed using OpenFOAM. The standard $k-\epsilon$ (with wall functions) and $\overline{v^2}-f$ (without wall functions) turbulence models were implemented as seen in [Hatcher and Vasconcelos, 2014]. The decision of using two RANS models, which had been previously implemented for GC flows [Mehdizadeh and Firoozabadi, 2009], created a more comprehensive analysis. The $k-\epsilon$ model is commonly used in a wide range of CFD applications while the $\overline{v^2}-f$ turbulence model is relatively new but offers more accuracy depending on the flow scenario [Mehdizadeh and Firoozabadi, 2009]. Both RANS models were used to analyze the proposed one-layer SWE model focusing on the GC front trajectory and average depth.

The mean velocity vector field ($\vec{u}$) satisfies the incompressible RANS mass and momentum equations:

$$\begin{aligned} \nabla \cdot \vec{u} &= 0 \\ \partial_t \vec{u} + \vec{u} \cdot \nabla u &= -\nabla P + \nabla \cdot [(\nu + \nu_t) \nabla \vec{u}] \end{aligned} \tag{3.17}$$

where P = mean pressure, ν = kinematic viscosity and ν_t = turbulent viscosity. The turbulent viscosity expressions are provided below for each turbulence model:

$$\nu_t = C_{\mu_{KE}} \frac{k^2}{\epsilon} \quad (k - \epsilon \text{ model}) \qquad \nu_t = C_\mu \overline{v^2} T \quad (\overline{v^2} - f \text{ model}) \tag{3.18}$$

where k = turbulent kinetic energy, ϵ = turbulent dissipation, v = turbulent stress normal to streamlines, T = turbulent time scale, $C_\mu = 0.22$ and $C_{\mu_{KE}} = 0.09$. The turbulent viscosity calculated with the $\overline{v^2} - f$ model (see Eq. 3.18) is more accurate at resolving turbulence near walls when compared to Direct Numerical Simulations and experiments [Mortensen et al., 2010]. For both RANS models, the following equations are used to compute k and ϵ:

$$\begin{aligned} \partial_t k + \vec{u} \cdot \nabla k &= P_k - \epsilon + \nabla \cdot \left[(\nu + \frac{\nu_t}{\sigma_k}) \nabla k \right] \\ \partial_t \epsilon + \vec{u} \cdot \nabla \epsilon &= \frac{C_{\epsilon 1} P_k - C_{\epsilon 2} \epsilon}{T} + \nabla \cdot \left[(\nu + \frac{\nu_t}{\sigma_\epsilon}) \nabla \epsilon \right] \end{aligned} \tag{3.19}$$

in which P_k is the production term and $C_{\epsilon 1}$, $C_{\epsilon 2}$, σ_k and σ_ϵ are standard $k - \epsilon$ coefficients. Compared to the $k - \epsilon$ model, the $\overline{v^2} - f$ turbulence model contains an additional equation for ($\overline{v^2}$) that improves accuracy near walls particularly for cases involving flow separation [Lien and Kalitzin, 2001]. In addition, an elliptic relaxation equation is required for $\overline{v^2} - f$ models because of nonlocal suppression of $\overline{v^2}$. These additional expressions for the $\overline{v^2} - f$ model are provided below [Durbin, 1991], [Durbin, 1995]:

$$\begin{aligned} \partial_t \overline{v^2} + \vec{u} \cdot \nabla \overline{v^2} &= kf - 6\overline{v^2} \frac{\epsilon}{k} + \nabla \cdot \left[(\nu + \frac{\nu_t}{\sigma_k}) \nabla \overline{v^2} \right] \\ L_{k\epsilon}^2 \frac{\partial^2 f}{\partial x_j \partial x_j} &= f + \frac{1}{T} \left[(C_1 - 6) \frac{\overline{v^2}}{k} - \frac{2}{3} (C_1 - 1) \right] - C_2 \frac{P_k}{k} \end{aligned} \tag{3.20}$$

where $L_{k\epsilon}$ is the turbulent length scale, kf is a pressure-strain term, and C_1 and C_2 are coefficients provided in [Lien and Kalitzin, 2001]. The production term (P_k) is computed from the expression [Durbin, 1995]:

$$P_k = \nu_t \left(\frac{\partial u_i}{\partial x_j} + \frac{\partial u_j}{\partial x_i} \right) \frac{\partial u_i}{\partial x_j} \tag{3.21}$$

and the turbulent time (T) and length ($L_{k\epsilon}$) scales are provided below [Lien and Kalitzin, 2001]:

$$T = \max \left(\frac{k}{\epsilon},\ C_T \left(\frac{\upsilon}{\epsilon} \right)^{1/2} \right) \qquad L_{K\epsilon} = C_L \max \left[\frac{k^{3/2}}{\epsilon},\ C_\eta \left(\frac{\upsilon^3}{\epsilon} \right)^{1/4} \right] \tag{3.22}$$

The coefficients for the RANS models were adopted from [Lien and Kalitzin, 2001]:

$$\begin{gathered} C_{\mu_{k\epsilon}} = 0.09, \quad C_\mu = 0.22, \quad C_{\epsilon 1} = 1.4 \left(1 + 0.05 \sqrt{k/\overline{\upsilon^2}} \right), \quad C_{\epsilon 2} = 1.9, \\ \sigma_k = \sigma_\epsilon = 1.3, \quad C_1 = 1.4, \quad C_2 = 0.3, \quad C_T = 6, \quad C_L = 0.23 \quad C\eta = 70 \end{gathered} \tag{3.23}$$

A dynamic time step was used with a maximum Courant number and time step of 0.5 and 1.0 s, respectively. 20,000 computational cells were used in the $k-\epsilon$ simulations: 500 longitudinal cells and 40 vertical cells (both uniform). The $\overline{\upsilon^2} - f$ model (without wall functions) requires a much finer grid than the $k-\epsilon$ model near the bed ($y^+ \approx 1$). For the $\overline{\upsilon^2} - f$ simulations, there were 500 computational cells in the longitudinal direction ($\Delta x = 6.0$ mm) and 80 cells in the vertical direction (40,000 total cells). The grid spacing in the vertical direction was increased by a factor of 20 toward the channel bottom while the longitudinal spacing was uniform. Rigid lid conditions were assumed for both 2D-RANS models, and the following expressions were used for wall BCs in the $\overline{\upsilon^2} - f$ model [Mehdizadeh and Firoozabadi, 2009]:

$$\vec{u} = 0, \qquad k = 0, \qquad \overline{\upsilon^2} = 0, \qquad \epsilon = \frac{2\nu k}{y^2}, \qquad f = 0 \tag{3.24}$$

3.5 Integral model approach to simulate air pocket motion in stormwater tunnels

For air pocket motion in circular conduits, the flow is three-dimensional and highly turbulent. Instead of resolving the details of the turbulence and air pocket interface, an integral model approach was formulated to focus on the leading edge trajectory and average pocket depth. For this numerical approach outlined in [Ungarish, 2009], a relationship between the air pocket/GC thickness and its propagation speed is utilized to update the location of the leading edge at each end of the air pocket. Integral models assume uniform flow depth at each time step while providing the average GC depth and front celerity. Because of this uniform depth assumption, integral models, which are referred to as "box models" [Ungarish, 2009], are much simpler to implement than SWE and NS models. The integral model formulations follow the work of [Hatcher et al., 2014] and [Chosie et al., 2014].

The integral model is developed for horizontal (no slope) flow conditions following the experiments conducted by [Chosie, 2013] (see Fig. 3.7). Figure 3.8 presents a schematic diagram of this modeling approach where x_0 and y_0 are respectively the initial length and thickness (measured from the pipe crown) of the air pocket. After the knife gate valves are fully opened, the air pocket spreads in both directions at unique velocities according to the leading edge celerity and relative pipe flow velocity. Front conditions relate the air pocket leading edge celerity and its thickness and offer a closure to the integral model along with the air phase continuity equation. The front conditions used in the integral model framework are adapted to account for pipe flow velocities following the rationale by [Hallworth et al., 1998]. The resulting front condition is:

$$u_f = \frac{dx_f}{dt} = F\sqrt{gD} + V_{flow} \tag{3.25}$$

where x_f is the distance traveled by the respective air pocket front, F is the local Froude number at the upstream and/or downstream air pocket front, D is the pipe diameter and V_{flow} is the background flow velocity.

Each front condition uses a different formulation to determine the value of F at the leading edge of the air pocket. The first front condition applies the theory by [Benjamin, 1968] in which there is a momentum balance solved at the air pocket leading edge. The control volume (CV) encloses the leading edge so that the flow is uniform and hydrostatic at the CV boundaries. This formulation considers surface tension following [Wilkinson, 1982]. After integrating Equation 3.25 and solving for x_f, the result is the first integral model considered in this work (referred to as $M1$):

$$x_f = (F\sqrt{gD} + V_{flow})(t_{new} - t_{old})$$

$$F = \left[\frac{\pi D^2 A_2 - \dfrac{2\pi D A_2 \sigma}{\rho g r_c} - 4A_2 \left(A_2 \cos\alpha + \dfrac{1}{6} D^2 \sin^3\alpha \right)}{\pi D^2 \left(\dfrac{1}{2}\pi D^2 - A_2 \right)} \right]^{1/2} \tag{3.26}$$

where t_{new} is the updated time step; t_{old} is the previous time step; $\alpha =$ is the pipe half-angle, with 2α as the angle subtended from the center of the pipe to the free surface; σ is the air-water surface tension; r_c is the leading edge radius of curvature; and A_2 is the cross-sectional flow area beneath the air pocket equal to $\left(\pi - \alpha + \frac{1}{2}\sin\alpha\right)\frac{D^2}{4}$.

The second integral model approach ($M2$) utilizes the front condition presented in [Vasconcelos and Wright, 2008], which in turn was based on the work by [Townson, 1991]. This front condition accounts for the curvature at the air pocket front and has the advantage of accounting for the depth change at the hydraulic jump that trails the leading edge of the gravity current. A limitation is that while this front condition formulation does not assume uniform air pocket thickness, the integral model makes this assumption. This has impacts in the accuracy of model predictions, as is shown in the Section 4.4. The expression for the 2^{nd} proposed integral model ($M2$) is:

$$x_f = (F\sqrt{gD} + V_{flow})(t_{new} - t_{old})$$

$$F = \frac{\pi - \alpha - \sin\alpha\cos\alpha}{\pi}\left[\frac{1 - \frac{1}{3\pi}\Big(3\sin\alpha + 3(\pi-\alpha)\cos\alpha - \sin^3\alpha\Big)}{\frac{A_2}{\pi}\left(2 - \frac{A_2}{\pi}\right)}\right]^{1/2} \tag{3.27}$$

Since there are initially two air intrusion fronts for the cases studied in this work, Equation 3.26 or 3.27 are solved twice at each time step. With the front velocities known, the locations of each front are updated (x_{fU} and x_{fD}) according to Figure 3.8. The methodology used to solve each leading edge location is identical except that the sign of U changes depending on the orientation of the background flow with respect to the front motion. One of the difficulties in this procedure is that x_f (x_{fU} or x_{fD}) is a function of α and vice versa. For the implementation utilized in this work, x_f was first computed from parameters determined at the previous time step. Then, α was updated using the following volume/continuity expression:

$$Vol = \frac{L_p D^2}{4}\left(\alpha - \frac{1}{2}\sin 2\alpha\right) \tag{3.28}$$

in which Vol and $L_p = x_0 + x_{fU} + x_{fD}$ are the air pocket volume and length, respectively. This nonlinear expression was solved at each time step using the iterative Newton-Raphson method with a tolerance for α of 10^{-5}. A schematic diagram for this integral model formulation is displayed in Figure 3.8.

Albeit relatively simple, the integral models formulated in this work account for drag, pressure forces and surface tension (M1), but there are still important limitations. The model formulation utilizes steady-state theory for the air cavity motion in which zero displacement is assumed at the stagnation point. The steady-state assumption is valid during the initial slumping stage, but the air pocket motion will diverge from steady-state theory in later stages of the propagation [Simpson, 1997]. In addition, as previously stated, the spatial

variation in depth is neglected. Finally, the adopted radius of curvature at the leading edge ($r_c = 0.0034\,m$) followed the work of [Wilkinson, 1982] in rectangular cross-sections, while results in this work were obtained in circular pipes. Results are validated with experiments conducted by [Chosie, 2013] for various pocket sizes and background flows in 101.6 mm pipes.

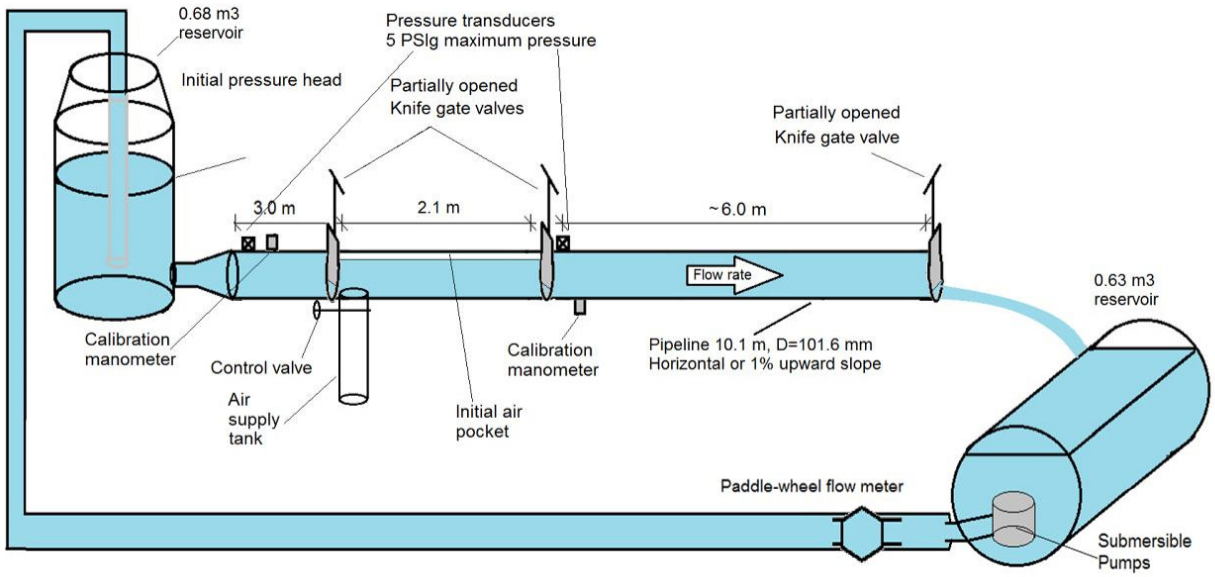

Figure 3.7: Schematic diagram of air pocket motion experiments conducted by [Chosie, 2013].

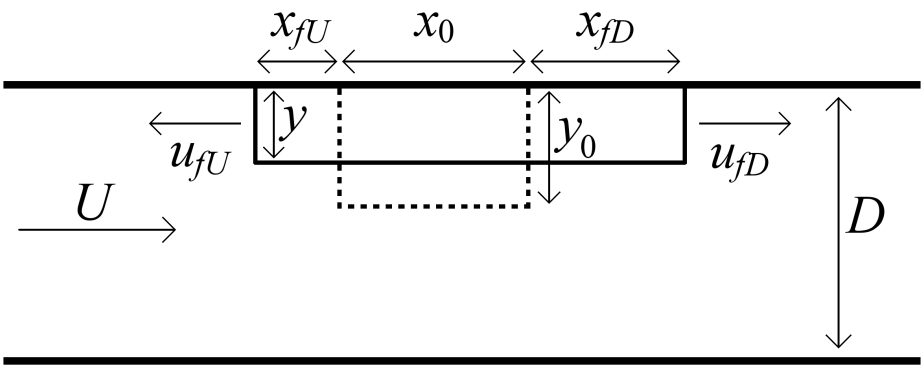

Figure 3.8: Schematic Diagram of the integral model approach used to simulate an air pockets propagating in circular pipes. The direction of u_{fD} is always positive while the sign of u_{fU} will vary depending on the magnitude of U and y/D.

Chapter 4

Results

4.1 Two-layer SWE applied to Boussinesq gravity currents

In [Hatcher and Vasconcelos, 2014] it was shown that the one-layer SWE, while able to predict GC front trajectories, was unable to accurately simulate the head of the current. One of the primary reasons for this discrepancy is the omission of the ambient layer momentum in the one-layer SWE formulation. To improve GC predictions, a shock-capturing two-layer SWE was developed (Section 3.2.2). The following sections analyze this two-layer model and the use of linear and nonlinear numerical schemes. MicroADV results obtained in lock-exchange experiments outlined in Section 3.1.3 were used to validate the SWE model. [Hatcher and Vasconcelos, 2013a] also compared the model with previous SWE models [Rottman and Simpson, 1983, Ungarish and Zemach, 2005] with good agreement. In Section 4.1.3 the effects of ambient crossflows are analyzed with respect to the two-layer SWE.

4.1.1 Numerical analysis of the two-layer SWE

The effect of the numerical scheme and time step size on the accuracy of the numerical model predictions are analyzed in Table 4.1. The assessment of the model accuracy is measured using two criteria: the difference between the experimental propagation time and the respective numerical prediction, and the continuity (mass balance) errors. The continuity error is defined as the percentage difference in denser fluid volume between the beginning of the simulation and the moment in time when the GC has propagated the entire length of the channel. Numerical results, all obtained with a 500-finite volume cell computational

domain (except where otherwise stated), are compared to experimental conditions ($x_0 = 76.2\,cm$, $h_0 = 40.6\,cm$, $\epsilon = 1\%$ and 2%), but results for larger density differences (not shown here for brevity) follow the same general trend.

This research determined that the selection of the numerical scheme does not have major importance on the overall accuracy provided Courant numbers are near unity. Results for nonlinear numerical schemes are stable for a larger range of Courant numbers, fractional depth and density differences, but finite difference SWE models performed well for most scenarios. The continuity errors were less than 0.7% for all numerical model results (Table 4.1), and the largest divergence between the measured and predicted propagation time was approximately 0.9%. The effect of the time step size was also analyzed by implementing two values for the Courant number: 0.9 and 0.3. These values were chosen because of the stability issues while applying the LxW numerical scheme. Although each numerical scheme presented in this work performed well for this lock-exchange scenario, the nonlinear numerical schemes performed better for smaller time steps yielded by lower Courant numbers, as anticipated. For the second-order accurate LxW finite difference method (FDM) scheme, the difference in propagation time was approximately $2 - 3$ sec depending on the Courant number. The difference in propagation time for the nonlinear schemes was less than 0.1 s. In addition, the continuity errors were consistently 0.2% less for the nonlinear schemes. The HLL and Roe schemes presented continuity errors consistently less than 0.1% when $Cr = 0.9$.

The LxW scheme produced minor oscillations throughout the slumping stage; however, this disadvantage was minor for the experiments conducted in this work compared to nonlinear schemes. The results for the HLL and Roe schemes were almost identical. A slight advantage was noticed with the HLL scheme with regards to computational time, but the Roe scheme was stable for a wider range of initial conditions. For the nonlinear Roe scheme, the Roe-Pike approach [Toro, 2001] was used to compute the Roe averages. The alternative approach to compute the Roe averages presented in [Glaister, 1988] performed almost

Table 4.1: Comparison between lock-exchange experiments and two-layer SWE model predictions for different time steps and front conditions. The gravity current time of propagation in the experiments was 93.67 s ($\epsilon = 1.0\%$) and 67.63 s ($\epsilon = 2.0\%$).

Numerical Model Predictions						
	$Cr = 0.9$			$Cr = 0.3$		
$\epsilon = 1.0\%$	LxW	HLL	Roe	LxW	HLL	Roe
GC propag. time (sec)	93.49	93.85	93.85	89.97	93.74	93.70
Error w/ experim. (%)	-0.20	+0.20	+0.19	-3.95	+0.08	+0.03
Continuity error (%)	+0.23	+0.02	+0.04	+0.95	+0.46	+0.48
	$Cr = 0.9$			$Cr = 0.3$		
$\epsilon = 2.0\%$	LxW	HLL	Roe	LxW	HLL	Roe
GC propag. time (sec)	68.00	68.26	68.26	65.44	68.18	68.15
Error w/ experim. (%)	+0.54	+0.94	+0.93	-3.24	+0.81	+0.77
Continuity error (%)	+0.23	+0.02	+0.04	+0.95	+0.46	+0.48

equally well for smaller Courant numbers but became unstable when the Courant number approached unity.

4.1.2 Experimental velocity measurements and corresponding numerical predictions

A comparison between the predicted and measured velocities at an intermediate point along the tank is presented in Fig. 4.1 for three different depths: $h^*_{ADV} = 0.063$, 0.125 and 0.188. A 9.14 m long, 12.5 cm wide flume was used in these experiments, and details of the experimental program are presented in [Hatcher, 2012]. Velocity measurements were performed with MicroADV probes sampling at a frequency of 20 Hz. Velocity values are normalized by $\sqrt{g'h_0}$ while time values are normalized by $x_o/\sqrt{g'h_0}$ (dimensionless variables are denoted with asterisks). The oscillations observed at the beginning of the velocity measurements were caused by the removal of the gate separating fresh and salt water. At about $t^* = 15$ there are sharp increases in velocity values that correspond to the arrival of the front at the MicroADV station (i.e. $x^* = x/h_0 = 7.68$). Velocity measurements indicate a gradual decline in the velocity after an initial peak that was caused by the front arrival. Measurements were continued after the GC advanced the entire length of the channel in order to

observe the reflections. As the reflected front reached the MicroADV probes, sharp negative values were generated for velocity denoting the arrival of the reflected front ($t^* = 40$) (see Fig. 4.1).

Figure 4.1 presents a comparison between the experimental measurements for the velocity and the predictions from the two-layer SWE model using the HLL scheme and Dual-Cell (DC) boundary condition with the modified Rottman and Simpson front condition and 200 computational cells. In Fig. 4.1 one notices good agreement between numerical simulations

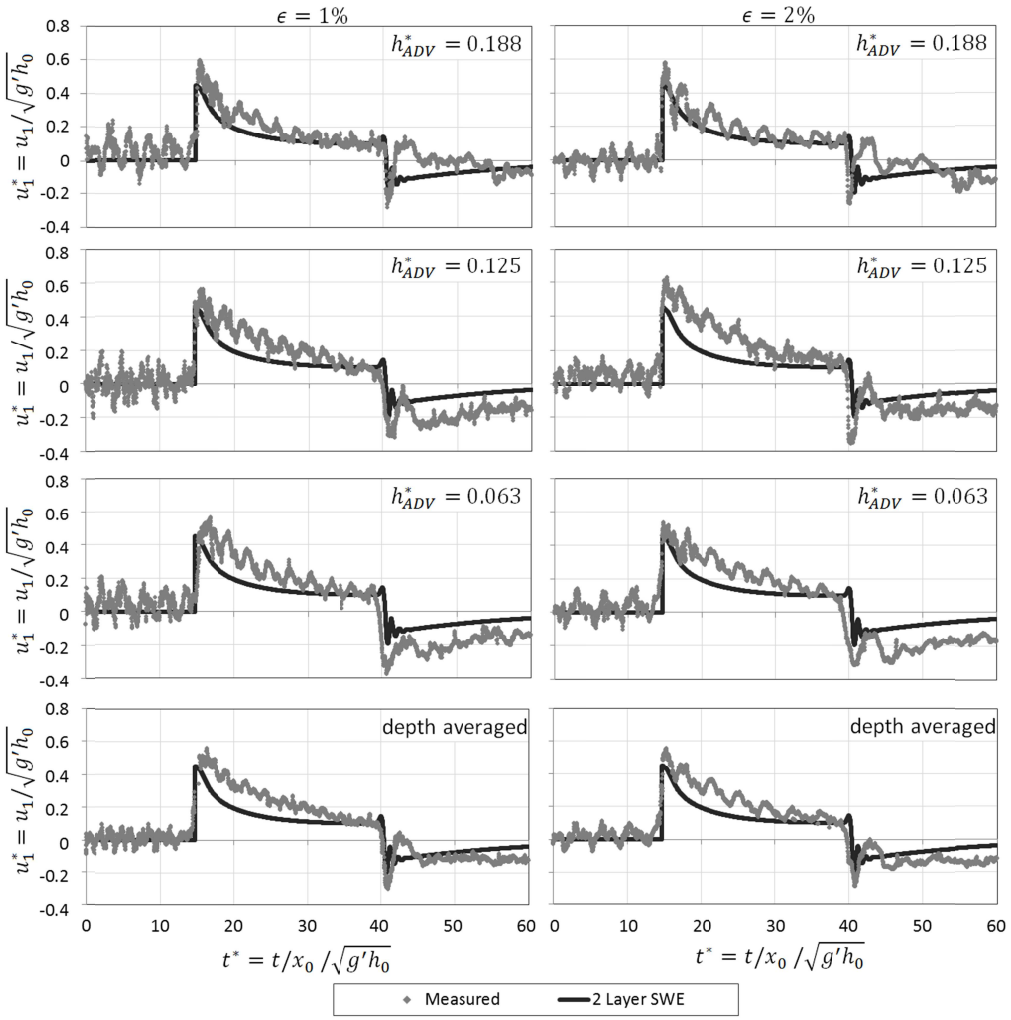

Figure 4.1: Denser fluid velocity hydrographs generated from experiments and the proposed two-layer SWE model with 200 computational cells. The experimental data is provided from MicroADV devices ($x^* = 7.68$) measuring at three different depths: $h^*_{ADV} = h_{ADV}/h_0 = 0.063, 0.125$ and 0.188. The experimental errors were $\Delta t^* = 0.01$, $\Delta u_1^* = 0.10\,(\epsilon = 1.0\%)$ and $\Delta u_1^* = 0.07\,(\epsilon = 2.0\%)$.

and the experimental data for $\epsilon = 1.0\%$ and $\epsilon = 2.0\%$. The theoretical front condition from Benjamin performs slightly better in reproducing the peak velocity magnitudes but performs far worse at estimating the arrival of the front. After the three depths were analyzed for $\epsilon = 1.0\%$ and $\epsilon = 2.0\%$ in Fig. 4.1, an arithmetic average was computed to determine the depth-averaged velocity profile. Since the MicroADV measurements were conducted at equal intervals ($2.5\,cm$) from the channel bottom to the depth behind the nose (around $10\,cm$), this type of averaging should converge to the depth-average solution. The results are promising and are presented at the bottom of Fig. 4.1.

The same approach was utilized for the upper MicroADV device ($h^*_{ADV} = 0.375, 0.625$ and 0.875) to analyze the velocities in the ambient fluid layer (the upper MicroADV was rotated 180^o with respect to the lower MicroADV so that the velocities were positive). The results are not quite as sharp (see Fig. 4.2) for the upper MicroADV because the wave amplitudes are closer in magnitude to the layered velocity. Also, the MicroADV probes are more successful at reading the saltwater, so the depth-averaged results are the focus for the ambient fluid. The HLL scheme with 200 computational cells was used again with the same boundary conditions as presented for the lower layer. The proposed two-layer model performs well at predicting the initial ambient front ($t^* \approx 15$) and the reflection ($t^* \approx 40$). Between $t^* \approx 20 - 30$, after the arrival of the initial ambient front, the ambient velocities computed with the two-layer SWE model under predict the results from the MicroADV much like for the GC layer. Overall, the proposed two-layer SWE model performs well at describing the velocities of both fluid layers.

4.1.3 Two-layer shallow water equations accounting for ambient crossflows

The ambient flow results are separated into two sections as discussed in Section 3.2.4: constant-volume and density intrusion gravity currents. The constant-volume simulations focus on a comparison between proposed and [Hallworth et al., 1998] two-layer SWE models. For density intrusion simulations, a comparison is made between the same proposed SWE

model (see Eq. 3.7) and 23 experiments performed by [Paez-Rivadeneira, 1997] with ambient crossflows (coflows and counterflows). As in previous sections, results are often displayed in terms of non-dimensional variables, which are denoted with an asterisk.

Constant-volume gravity currents

The initial conditions for the constant-volume simulations were chosen based on the results presented in [Hallworth et al., 1998]. The length parameters are normalized by the initial depth (h_0): $h^* = 1$, $L^* = 14$, $x_0^* = 1$ in which the left side of the current is located 7.5 units from the beginning of the tank (see Fig. 4.3). The depth ratio ($h_0/H = 0.25$) is large enough so that the ambient velocity is important for the GC momentum but small enough to avoid shocks [Hallworth et al., 1998]. As stated in the methodology section, the initial velocity of the denser fluid is zero. The ambient velocity ($U^* = 0.1$) is moving to

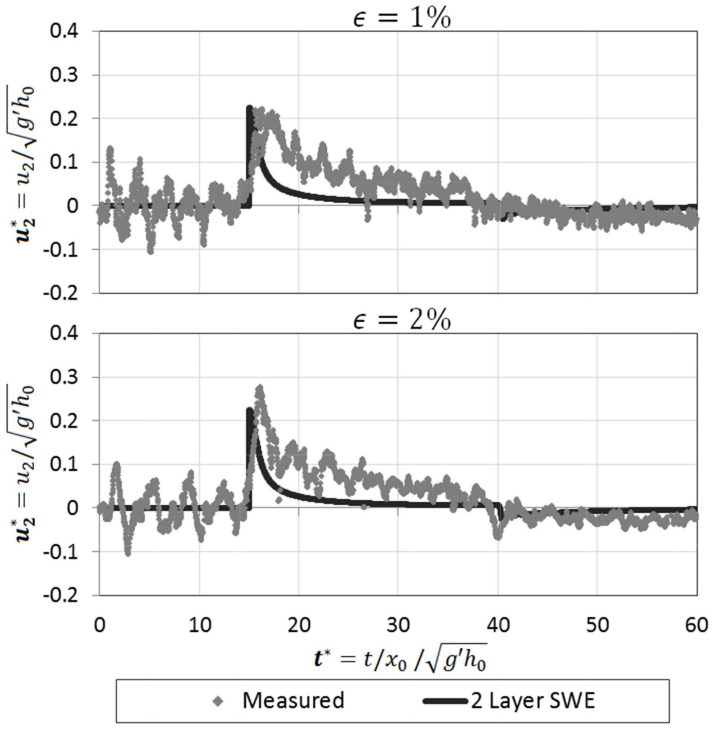

Figure 4.2: Ambient fluid depth-averaged velocity hydrographs generated from experiments and the proposed two-layer SWE model with 200 computational cells. The experimental data ($\epsilon = 1.0\%$ and 2.0%) is provided from MicroADV devices at $x^* = 7.70$. The experimental errors were $\Delta t^* = 0.01$, $\Delta u_2^* = 0.10$ ($\epsilon = 2.0\%$) and $\Delta u_2^* = 0.07$ ($\epsilon = 2.0\%$).

the left so that the right front moves slower and with greater depth than the left GC front. The velocities and times are normalized by $\sqrt{h_0 g'}$ and $\sqrt{h_0/g'}$, respectively. The simulation consisted of 500 computational cells with a Courant number of 0.9.

At the beginning of the simulation ($t* = 0.5$), sharp depth gradients exist in the middle of the solution domain due to the depression wave generated from the GC release. The depth results using the HLL scheme in Fig. 4.3a) compare fairly well with [Hallworth et al., 1998], but the maximum depth is underestimated due to first order accuracy. The Lax-Wendroff second-order accurate FDM scheme in Fig. 4.3b) performs better for this feature. For the rest of the simulation, both numerical schemes result in very similar depth profiles and almost identical front trajectories.

Throughout the simulation the trajectory of the left front compares very well between [Hallworth et al., 1998] and proposed SWE models. The results for the right front compare

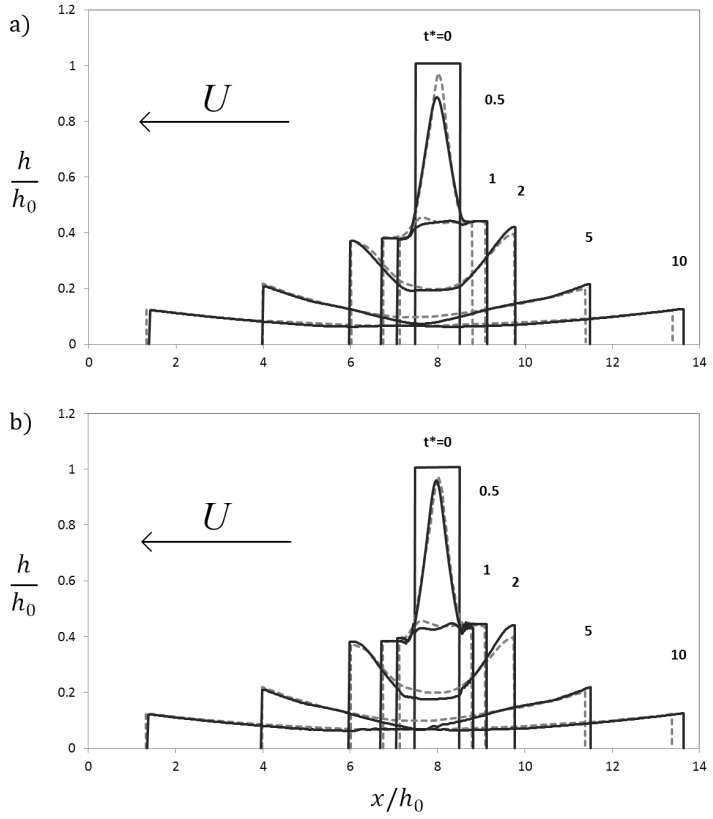

Figure 4.3: Superimposition of [Hallworth et al., 1998] (dotted line) and proposed (dark line) two-layer SWE models using a) HLL FVM and b) LxW FDM schemes.

well to one another but start to diverge at $t^* \approx 10$. This small divergence is independent of the front condition since both models use the HS expression. The cause of error in trajectory is believed to stem from minor differences in the mathematical model and/or in the front BC solution strategy. There are differences between the shock-tracking technique used in the proposed model and the characteristic approach from [Hallworth et al., 1998] using interpolation. The continuity error for the proposed model was consistently around 0.6%.

Density intrusion gravity currents

The proposed SWE model predictions were utilized to compare the density intrusion simulations in terms of the front velocity experimentally measured at a specified location $4.0 - 4.5$ m away from the injection point. The velocity was measured by visually tracking the location of the GC front using a stop watch with a precision of 0.01 seconds. Like the constant volume simulations, 500 computational cells were used with a Courant number of 0.9, and the continuity error was consistently less than 1%.

The front velocity results compare fairly well with the experiments for both coflows (Fig. 4.4a) and counterflows (Fig. 4.4b). In coflow simulations the ambient velocity is in the same direction as the GC advance. All nine of the experimental results conducted by [Paez-Rivadeneira, 1997] with ($0.16 \leq h_0/H \leq 0.23$) are analyzed. The results in Fig. 4.4a) compare very well to one another. Initially, the discrepancy between predictions and experiments was larger, but the front condition was altered based on observations from [Simpson and Britter, 1980]. They determined from their experiments that U is approximately 60% of the mean velocity in the channel. [Hallworth et al., 1998] utilized this methodology as well in their model and stated that the GC front only experiences around 60% of the mean ambient velocity in their experiments as well. Once this change was made to the GC front condition (Eq. 3.8), the SWE results compare fairly accurately to the experimental results presented in [Paez-Rivadeneira, 1997].

The results for the counterflow simulations (Fig. 4.4b) compare well also, but there are a few outliers with less accuracy. Similar to the coflows, the counterflow results improved substantially when the front velocity was altered with an accurate value for the ambient velocity. All 14 counterflow experiments conducted by [Paez-Rivadeneira, 1997] at a sampling location of 4.5 m from the source were analyzed. The results are very accurate for all but $3-5$ runs in which the front velocity is slightly overestimated by the SWE model.

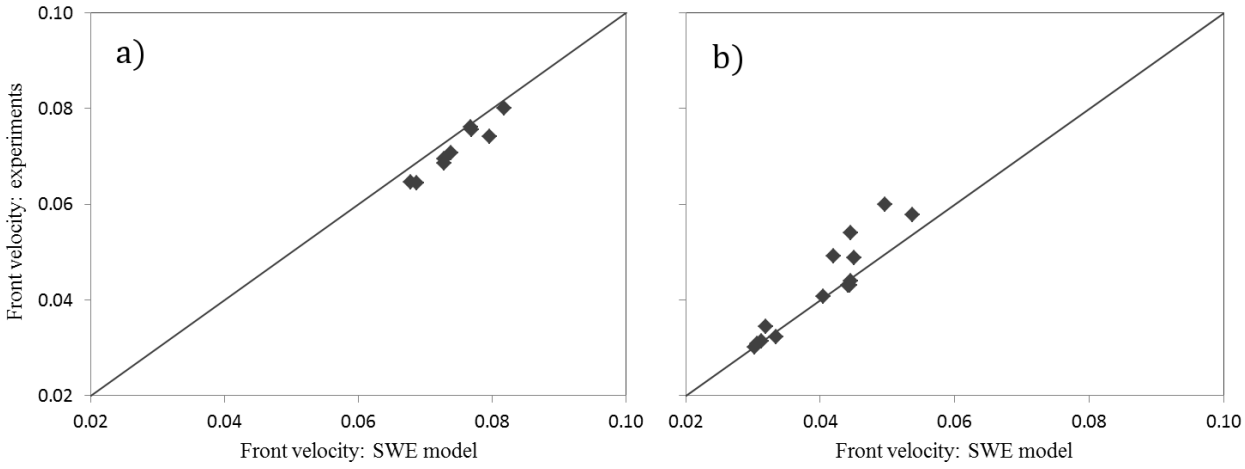

Figure 4.4: Front velocity (ms^{-1}) comparison between [Paez-Rivadeneira, 1997] experiments and proposed two-layer SWE model for a) coflows and b) counterflows.

4.2 Alternatives for flow solution at the GC leading edge

The three leading edge BC solution strategies discussed in Section 3.3 are analyzed for constant-volume and density intrusion gravity currents. In computing the GC leading edge location, the BC methods are fairly indistinguishable [Hatcher and Vasconcelos, 2014]. However, the effects of computational time and continuity error can be significant and are analyzed in the following section. This section follows [Hatcher and Vasconcelos, 2014] where the one-layer SWE model was validated with the numerical model from [Ungarish, 2009] and experiments by [Paez-Rivadeneira, 1997].

4.2.1 Constant-volume gravity currents

To analyze the front BC solution strategies for constant-volume GC, h_0 was adjusted so that $(0 < \phi \leq 0.5)$ while the following initial conditions were constant: $H = 1$ m, $x_0 = 1$ m, $L = 10$ m. For Boussinesq, constant-volume gravity currents, the propagation is a function of the depth ratio [Ungarish, 2009]. Thus, the deep ambient ($\phi \approx 0$) and critical condition ($\phi = 0.5$) scenarios were chosen to generate the data in Tables 4.2 and 4.3.

In order to compare the front BC solution strategies, continuity errors, time steps and computational times were quantified. The continuity error (negative values equate to mass lost) is computed from the difference between initial ($x_{LE} = x_0$) and final ($x_{LE} = L$) GC volumes. Results for continuity error and computational times are shown in 4.2 ($\phi \approx 0$) and Table 4.3 ($\phi = 0.5$) for the tested range of discretization sizes. Because the front location is changing within the solution domain, the number of discretization cells is a maximum value that represents the number of cells at $x_{LE} = L$. Computations were carried out until the leading edge interface was at position $x/x_0 = 10$ or until the computational time reached one hour. The number of time steps for each front BC solution strategy was almost identical regardless of discretization size, which allowed for a more accurate computational time comparison. In addition, GC front trajectory results were very similar between each BC strategy.

Table 4.2: Comparison between measured continuity errors and computational time for STI, GOC and DC strategies - constant volume GC flows, deep ambient condition ($\phi \approx 0$).

Method	No. of cells	100	200	500	1000	5000	10000
STI	Cont. error (%)	-7.66	-3.77	-1.49	-0.74	-0.15	-0.08
	Comp. time (sec)	0.44	0.69	1.78	3.87	38.02	129.47
	No. of time steps	180	363	911	1824	9131	18265
GOC	Cont. error (%)	-0.48	-0.10	+0.15	+0.12	+0.05	NA
	Comp. time (sec)	0.61	1.22	5.04	19.48	2469	>1 hr
	No. of time steps	182	365	913	1826	9133	NA
DC	Cont. error (%)	-6.17	-2.56	-1.02	-0.51	-0.10	-0.05
	Comp. time (sec)	0.17	0.96	2.33	5.11	44.01	144.09
	No. of time steps	181	363	911	1825	9132	18265

Table 4.3: Comparison between measured continuity errors and computational time for STI, GOC and DC strategies - constant volume GC flows, critical condition ($\phi = 0.5$).

Method	No. of cells	100	200	500	1000	5000	10000
STI	Cont. error (%)	-10.20	-5.90	-3.64	-2.84	-2.34	-2.27
	Comp. time (sec)	0.32	0.66	1.77	3.90	38.81	137.48
	No. of time steps	195	394	990	1984	9939	19882
GOC	Cont. error (%)	-4.08	-1.53	-0.46	-0.19	-0.02	NA
	Comp. time (sec)	0.39	0.97	4.84	20.64	2586	>1 hr
	No. of time steps	198	397	993	1988	9942	NA
DC	Cont. error (%)	-6.96	-3.58	-1.44	-0.71	-0.15	-0.07
	Comp. time (sec)	0.35	0.72	1.87	4.18	40.25	127.44
	No. of time steps	196	396	992	1986	9941	19884

The results for both initial conditions indicate a similar trend for each BC approach. The Grid-of-Characteristics (GOC) approach results consistently yielded the smallest continuity error, yet this method is clearly the most computationally intensive. The Specified-Time-Intervals (STI) approach resulted in the largest continuity error, particularly for larger depth ratios, but had the smallest computational time. The DC approach computational time was slightly larger than the STI method, albeit with much smaller continuity errors especially for larger depth ratios.

4.2.2 Density intrusion gravity currents

For the density intrusion GC simulations, the three BC approaches were tested for the conditions presented in the experimental work by [Paez-Rivadeneira, 1997]. The experimental apparatus length was 10 m, and the advancing front velocity was experimentally measured at station $x = 4$ m from the denser fluid inlet. Various conditions were tested involving many injection flow rates per unit width (uh_{in}), depth ratios at the inlet (ϕ_{in}) and reduced gravity (g'). In the present study, a comparison between the approaches to solve flows at the leading edge is performed for 20 of the tested conditions. The ranges of experimental values considered in this comparison were: $\phi_i n$ from $0.10 - 0.417$, g' from $3.60 - 8.82$ cm s^{-2}, and uh_{in} from $23.85 - 49.87$ cm^2 s^{-1}. The resulting range of front velocities observed in this work was $3.81 - 6.43$ cm s^{-1}.

For all tested conditions, the continuity errors were relatively small with the largest around 3% and in most cases 1%. To be consistent with the reported experimental conditions, both depths and flow rates were enforced at the apparatus boundary. Continuity errors and computational times are shown for two of the simulated cases in Fig. 4.5. Results follow approximately the same general trend observed in the previous example involving constant-volume GC flows. Continuity errors were in general largest for the STI approach and smallest for the GOC approach. Computational time, on the other hand was smallest for the STI approach, but results with the DC approach are comparable especially for finer discretization. GOC results required much larger time when the number of grid cells were $5,000$ or above.

One may notice that the increase of computational cells for case (b) in Fig. 4.5 has not resulted in zero continuity errors in any of the tested solutions. This lack of convergence has to do with the enforcement of h and uh at the system boundary. In the context of open-channel flow problems, it is known that such practice leads to accuracy issues when a characteristic line from the domain arrives at the system boundary. An alternative solution at the system boundary that enforced only the inflow and used a $C-$ characteristic line was used in such cases, and continuity errors were much reduced (results not shown for

brevity). However, to maintain consistency between the 20 cases selected for comparison, as well as with the reported experimental conditions, all results shown enforced these two flow variables.

A comparison between experimentally measured front velocities and model predictions using the three solution approaches for the flow at the leading edge is shown in Fig. 4.6. All simulations were obtained with a 100-cell grid, as these front velocity results were not too dependent on the discretization size. One notices that there is generally good agreement between predicted and measured front velocities, which were not dependent on the selected approach to solve flow velocities at the GC leading edge. The one-layer SWE results displayed little bias compared to the experimental measurements.

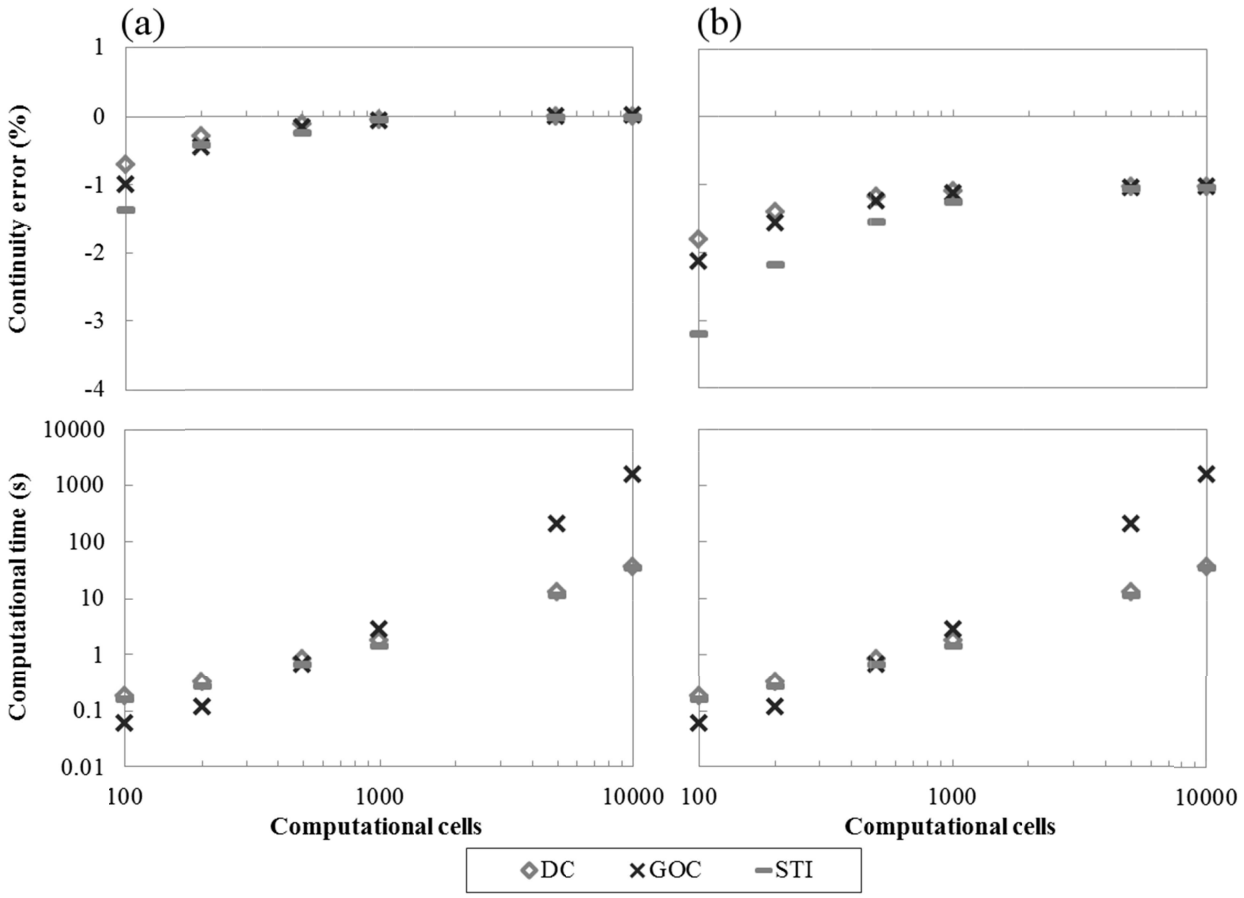

Figure 4.5: Continuity error and computational time comparison for density intrusion GC flows using the DC, GOC and STI approaches to compute flows at leading edge region. For the experimental conditions, (a) $\phi = 0.16$, $g' = 6.75$ cm s^{-2}, $u_{in} = 7.28$ cm s^{-1} and (b) $\phi = 0.40$, $g' = 6.17$ cm s$^{-}2$, $u_{in} = 5.22$ cm s^{-1}.

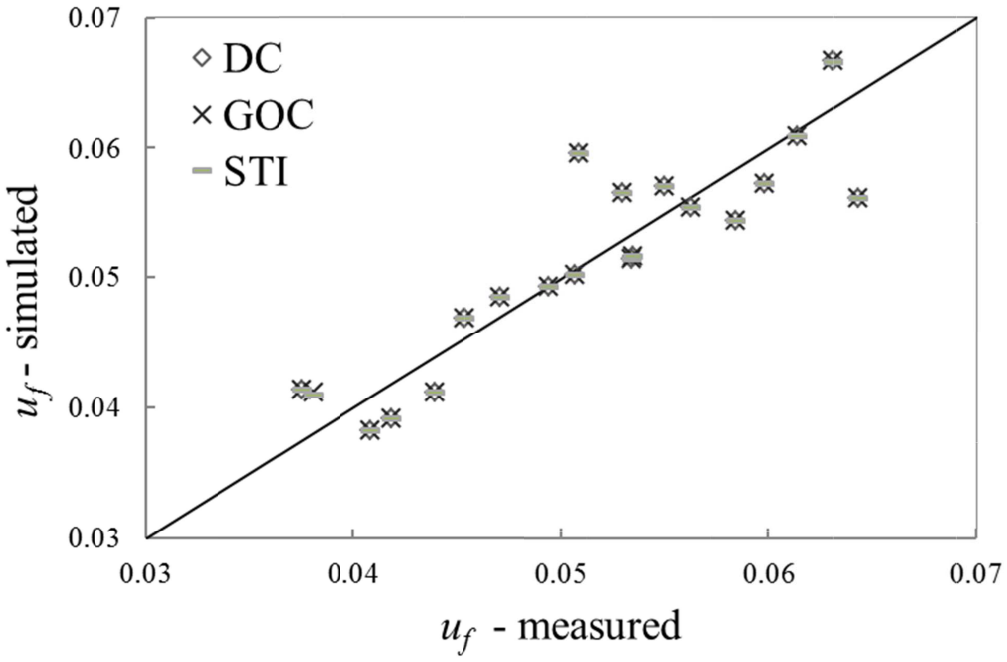

Figure 4.6: Front velocity (ms^{-1}) comparison between single-layer SWE model and density intrusion experiments conducted by [Wright and Paez-Rivadeneira, 1996].

4.3 One-layer SWE and 2D RANS comparison for lock-exchange gravity currents

Results presented thus far indicated that computational effort for GC flows solved with the SWE is generally small even for fine discretization, particularly when DC or STI methods to solve flows at the leading edge are used. While continuity was mostly preserved in calculations, a pertinent question is how well those models represent the advance of GC flows over time. SWE models are clearly unable to describe the detailed flow structure for GC flows due to their one-dimensional nature, so one anticipates that the GC shape cannot be accurately represented. However, one question is whether the trajectory of the leading edge is well predicted over the slumping and self-similar stages of the GC flow.

To address this question a three-way comparison is performed for constant-volume GC between experimental results presented by [Marino et al., 2005], predictions from the SWE model (using the DC strategy) and 2D-RANS modeling strategies presented in the methodology. For the CFD model, the choice of $k-\epsilon$ turbulence model was motivated by simplicity and popularity, whereas $\overline{v^2}-f$ model was chosen because of improved accuracy in comparison with other RANS models [Mehdizadeh and Firoozabadi, 2009]. Only constant-volume GC flows are used in this comparison between SWE and 2D-RANS models.

The partial depth experimental results from [Marino et al., 2005] were used for comparison and are displayed in Figs. 4.7, 4.8, and 4.9. They were able to determine the equivalent GC depth with a lighting technique outlined in [Dalziel, 1993] in which the saltwater mass was measured within 2% accuracy. GC flow conditions represent the case for $x_0 = 0.1$ m, $L = 3$ m, $h_0 = 0.16$ m, $H = 0.4$ m, $\phi = 0.4$ and $g' = 0.098$ ms^{-2}.

According to the GC profiles displayed in Fig. 4.7, the SWE model predicts the early stages of front location with fair accuracy in comparison with [Marino et al., 2005] experiments, with better accuracy than the 2D RANS simulation using the $\overline{v^2}-f$ model. As shown in Fig. 4.7d for $t = 40.0$ s, 2D-RANS predictions at the leading edge of the GC exceed the SWE prediction by a slight amount. As indicated in Fig. 4.8, the same trend

is observed when the $k-\epsilon$ model is considered, except that at latter stage there is better agreement between this 2D-RANS model and the SWE prediction. However, as indicated in the trajectories presented in Fig. 4.9, the best representation of the leading edge location measured in the experiment at $t = 40.0$ s ($t^* = 50.1$) was yielded by the $\overline{v^2} - f$ model.

As indicated in Figs. 4.7 and 4.8, SWE predictions fail to present an accurate depiction of gravity current head throughout the different stages of the flow propagation, particularly at the earlier stages. Both $\overline{v^2} - f$ and $k-\epsilon$ models yield a fair representation of the shape

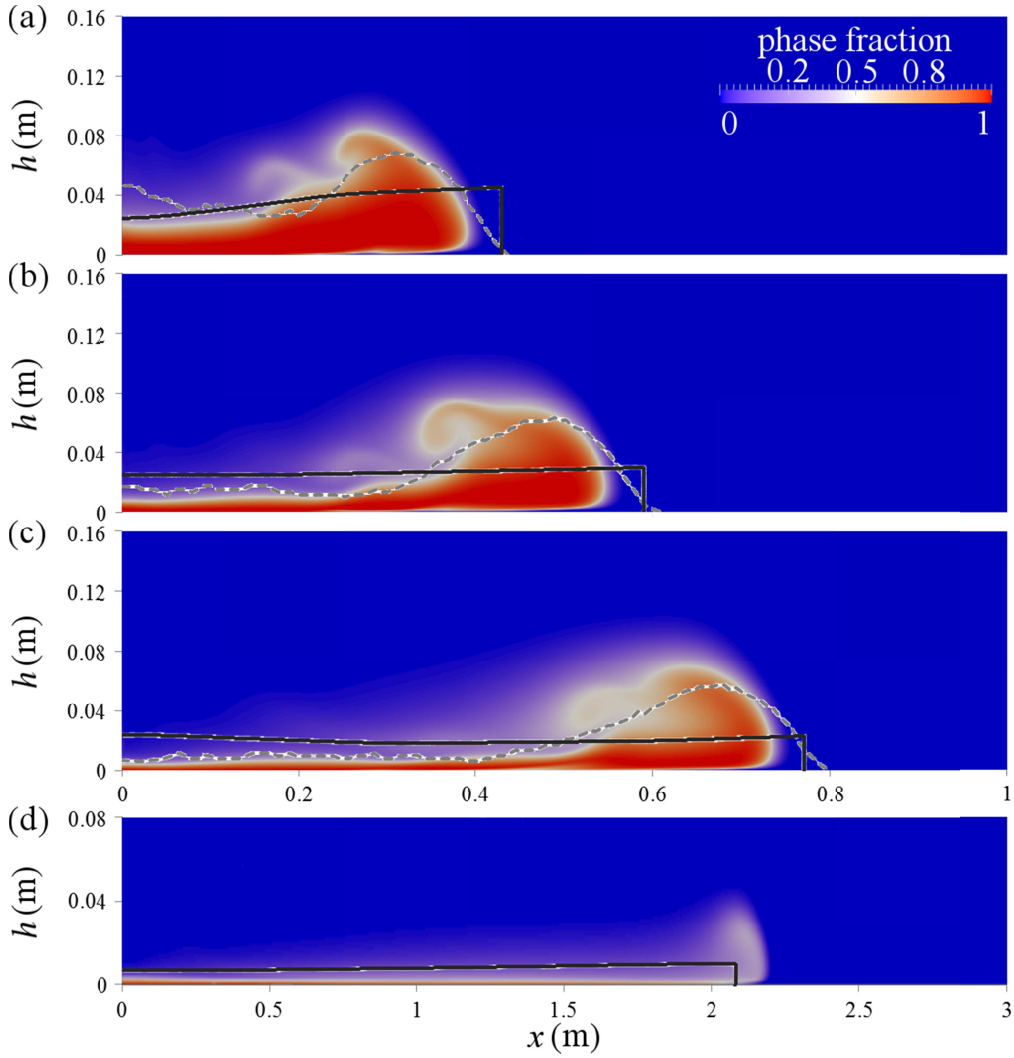

Figure 4.7: Gravity current propagation comparison between (solid line) SWE and 2D RANS ($\overline{v^2} - f$) simulations and experiments (dashed line) by [Marino et al., 2005] for (a) $t = 4.5$ s, (b) $t = 6.9$ s, (c) $t = 9.9$ s, and (d) $t = 40.0$ s: $x_0 = 0.1$ m, $L = 3$ m, $h_0 = 0.16$ m, $H = 0.4$ m, $\phi = 0.4$ and $g' = 0.098$ ms^{-2}.

of the GC leading edge. The former presented a better representation of the flow conditions behind the leading edge, as the $k - \epsilon$ model (with wall functions) seemed to excessively diffuse this region upstream of the GC head.

The front trajectories are compared in Fig. 4.9 for the two numerical modeling alternatives and the same [Marino et al., 2005] experiment analyzed in Figs. 4.7 and 4.8. All of the numerical models predict the location of the front reasonably well before the end of the initial slumping stage ($t^* \approx 18$). In comparison with the experiments, the $\overline{v^2} - f$ model

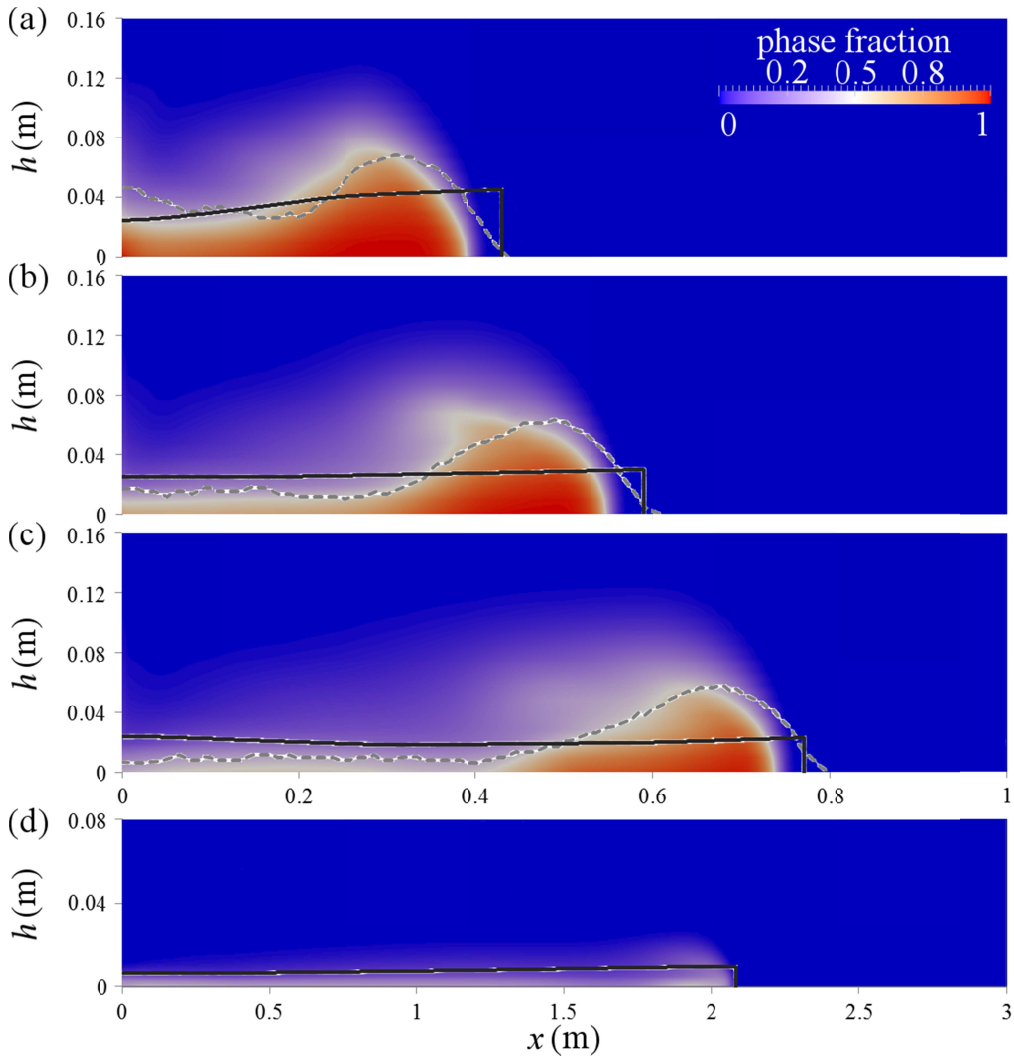

Figure 4.8: Gravity current profile comparison between (solid line) SWE and 2D RANS ($k - \epsilon$) simulations and experiments (dashed line) by [Marino et al., 2005] for (a) $t = 4.5$ s, (b) $t = 6.9$ s, (c) $t = 9.9$ s, and (d) $t = 40.0$ s: $x_0 = 0.1$ m, $L = 3$ m, $h_0 = 0.16$ m, $H = 0.4$ m, $\phi = 0.4$ and $g' = 0.098$ ms^{-2}.

clearly is the most accurate within the later self-similar stage. The SWE model simulated accurately the initial slumping stage and fairly accurately the unsteady self-similar phase (a closer approximation than $k - \epsilon$ model results).

For this constant-volume GC flow, the computational times were compared on the same computer with a 2.40 GHz clock CPU. The SWE model simulation time was 6.4 seconds. The $k - \epsilon$ model with wall functions yielded results in slightly over 20 minutes (1,215 seconds) while the $\overline{v^2} - f$ model had the longest computational time of almost 5 hours (17,251 seconds). These times indicate that depending on the modeling objectives there may be some advantages in using a simpler SWE simulation for GC flows. This could be the case when a large number of simulations are required, as exemplified in parametric studies such as the ones conducted by [Ungarish and Huppert, 2002] and [Hogg et al., 2005].

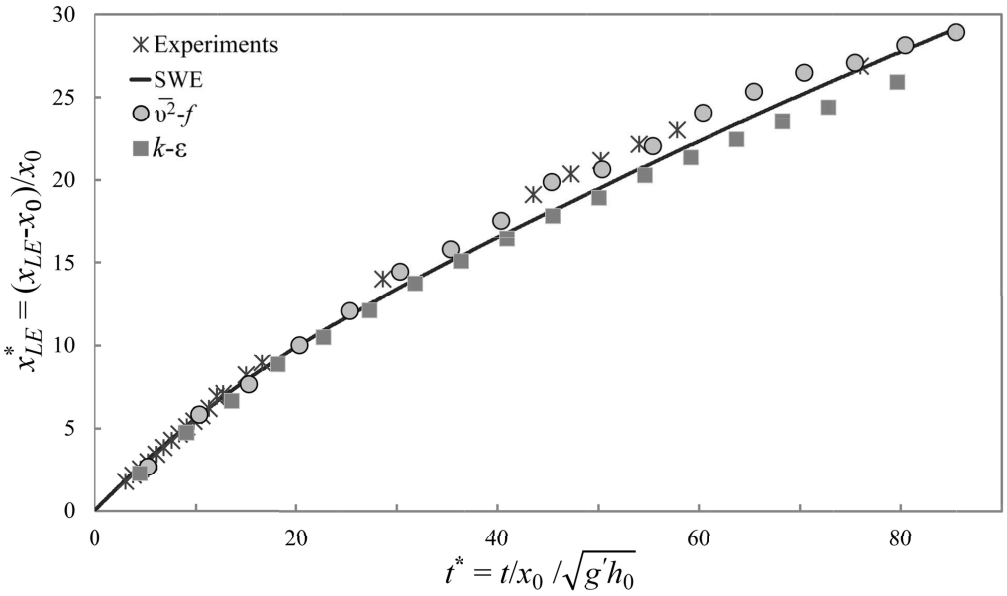

Figure 4.9: GC front trajectory comparison between SWE and 2D RANS simulations and [Marino et al., 2005] experiment.

4.4 Air pocket motion in closed conduits

To this point, all of the simulations have involved Boussinesq flows. As discussed in Section 3.5, two integral models were formulated for non-Boussinesq flows in circular conduits. The proposed integral model was tested with four different air pocket volumes and background flow rates, all involving horizontal pipe conditions. The model alternatives ($M1$ and $M2$) discussed in the Methodology were compared to [Chosie, 2013] experiments to analyze leading edge trajectories. Both alternatives were simple to implement and involved relatively small computational times. Thus, simulations were concluded in a fraction of a second.

The limitation of slope was due to the inability to obtain accurate and systematic experimental measurements of air pocket fronts. Another limitation of the numerical model is that comparisons only involved downstream moving fronts when ambient flows were present. This is mostly due to the fact that the upstream moving fronts lasted briefly as they were quickly sheared by ambient flows. Such conditions yielded a limited amount of experimental data points and prevented a comparison between experimental and model results.

The air cavity front trajectories for horizontal flow experiments are compared to both numerical model alternatives ($M1$ and $M2$) in Fig. 4.10. The pocket front coordinate (x) was normalized by the initial air pocket length (x_0) and the time by ($x_0/\sqrt{gD}$). The experimental results are clearly affected by the background flow rate in which the air cavity front velocity is governed by Eq. 3.25 as described in [Hallworth et al., 1998]. The effect of air pocket volume on front velocity in the tested conditions was not as important as the ambient velocity.

Figure 4.10 indicates that in the absence of background flow, $M1$ consistently compared better to experimental results, and this agreement was considered good. On the other hand, $M2$ consistently underestimated the air pocket front velocity, and this error increased for larger air pocket sizes. $M2$ predictions were more accurate or comparable to $M1$ predictions only for cases involving smaller air pocket volumes ($Vol^* = 1.2$ and $Vol^* = 2.2$) in the presence of higher background flows. The accuracy of $M1$ appears unaffected by different

background flows and pocket sizes. These results indicate that the surface tension parameters presented in [Wilkinson, 1982] for rectangular pipe cross sections were adequate for circular pipes.

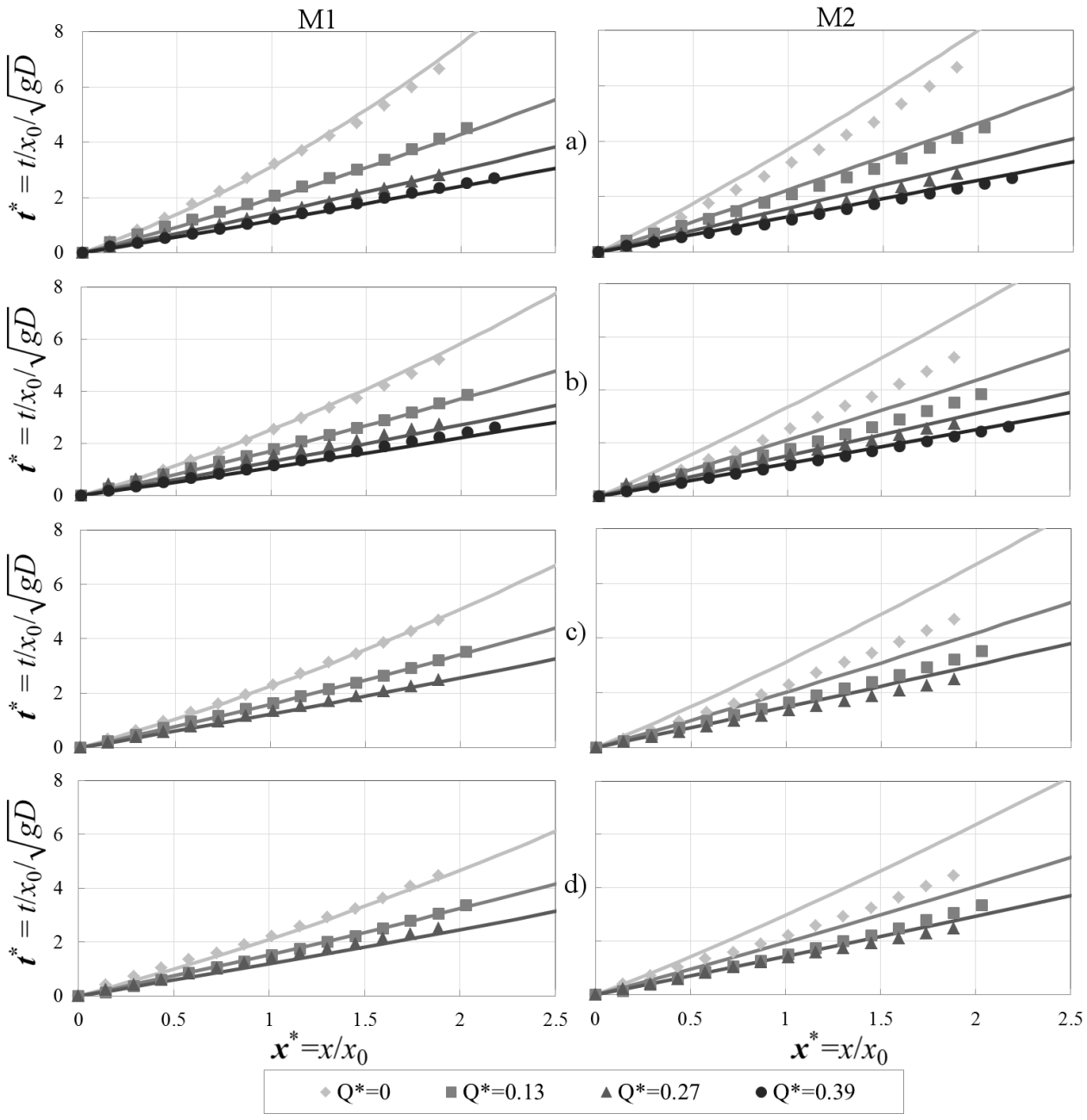

Figure 4.10: Air pocket front trajectory comparison between experiments and both integral models for various background flows and pocket volumes: a) $Vol^* = 1.2$, b) $Vol^* = 2.2$, c) $Vol^* = 3.1$, and d) $Vol^* = 4.1$. The solid lines represent the integral model predictions, and the data markers represent experimental values.

Table 4.4: Cavity Froude number ($F = u_f/\sqrt{gD}$) comparison for the largest and smallest air pocket volumes tested with various background flows.

$Q^* = Q/\sqrt{gD^5}$	0	0.13	0.27	0.39
	$Vol^* = 1.2$			
Experiments	0.284	0.451	0.672	0.804
M1 prediction	0.268	0.467	0.664	0.826
M2 prediction	0.253	0.431	0.617	0.773
	$Vol^* = 4.1$			
Experiments	0.419	0.594	0.751	N/A
M1 prediction	0.427	0.612	0.809	0.972
M2 prediction	0.323	0.496	0.683	0.840

While experimental observations indicated that the initial stages (t^* <2) of the air pocket propagation were characterized by a gradual increase on the air pocket celerity, both modeling approaches neglected this effect and yielded larger celerity values at these initial seconds of the flow. As shown in Figure 4.11, both model alternatives assume a larger celerity value than what was measured in these initial stages of the flow. This discrepancy is attributed to the limitations and simplifying hypothesis in the gravity current integral model. After $t^* > 2$, results from $M1$ are fairly close to the observations from tested conditions. Results yielded by the $M2$ model compared well only with the the smallest air pocket tested $Vol^* = 1.2$.

The accuracy of air pocket velocity predictions are reflected in a comparison between measured and predicted cavity Froude numbers ($F = u_f/\sqrt{gD}$), which are provided in Table 4.4. The smallest ($Vol^* = 1.2$) and largest ($Vol^* = 4.1$) air pocket volumes from experiments were selected for the comparison. The front velocity (u_f) was computed from the average velocity between $t^* = 0$ and $t^* \approx 2.5$. $M1$ was more accurate of the two integral models for each one of the experiments tested in this comparison. This model underpredicted F values by only 0.1% for $Vol^* = 1.2$ experiments while overpredicting results in $Vol^* = 4.1$ experiments by 4.2%. $M2$ underpredicted F values by an average of 11.5% with larger discrepancies occurring for larger air pockets and smaller background flows.

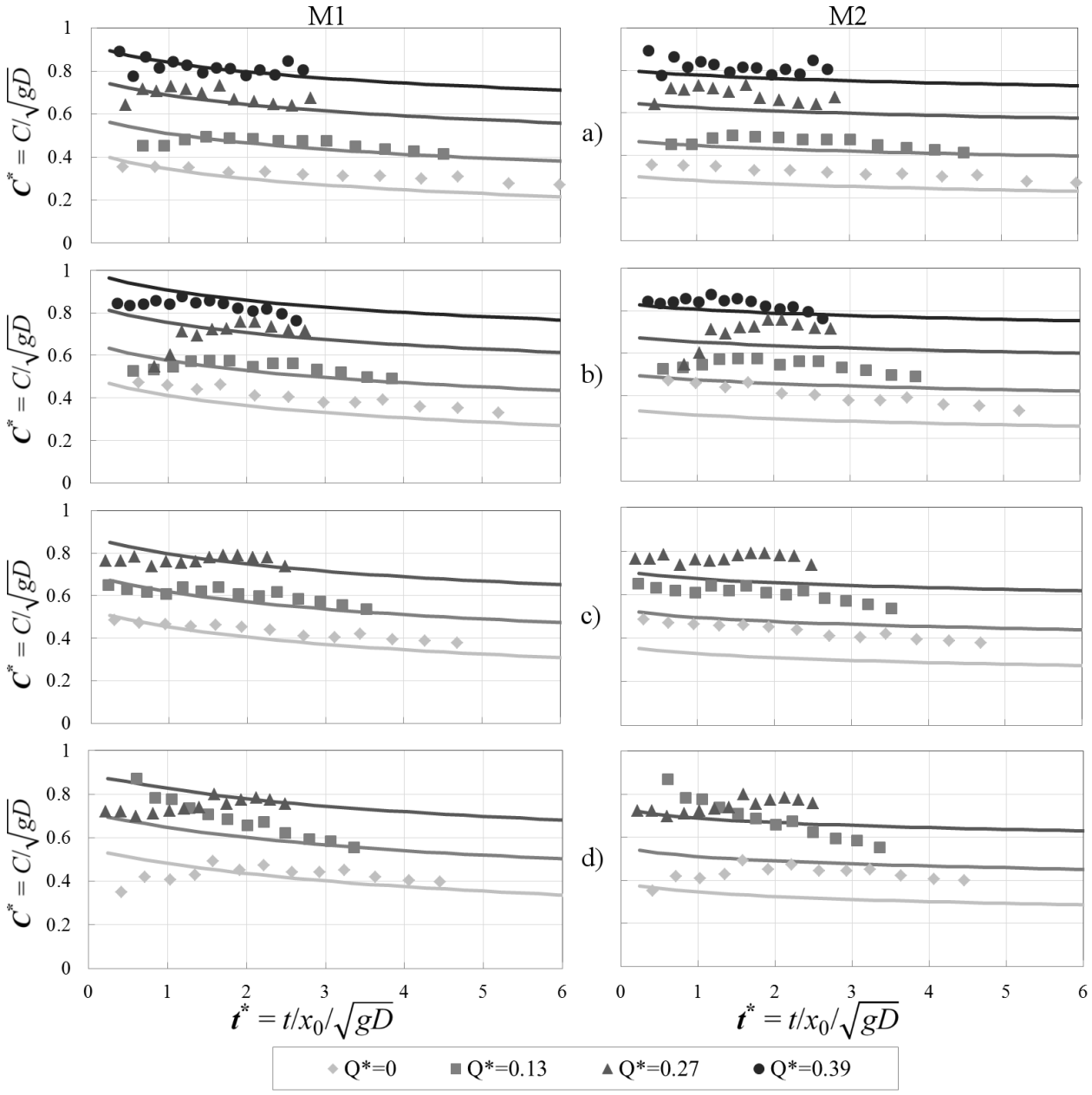

Figure 4.11: Air pocket front celerity comparison between experiments and both integral models for various background flows and pocket volumes: a) $Vol^* = 1.2$, b) $Vol^* = 2.2$, c) $Vol^* = 3.1$, and d) $Vol^* = 4.1$. The solid lines represent the integral model predictions, and the data markers represent experimental values.

Chapter 5

Conclusions

The first part of this research focused on shock-capturing shallow water equation (SWE) models to simulate lock-exchange gravity currents. Experiments were conducted to analyze the use of MicroADV devices focusing on Boussinesq currents. The SWE model was tested with these ADV results and superimposed with model results from [Rottman and Simpson, 1983] and [Ungarish and Zemach, 2005]. The conclusions are summarized below:

- The proposed SWE is similar to shock-capturing models used to describe free-surface bores. Non-linear finite volume schemes (HLL and Roe) were successfully implemented, and their performance was better (in terms of continuity errors and resolving discontinuities) than finite-difference alternatives (see [Hatcher and Vasconcelos, 2013a] for details).

- The two-layer SWE model can be rewritten in conservative and divergent format in which the ambient layer influences are incorporated as source terms, rendering the implementation into finite volume method (FVM) approaches simple and accurate.

- A shock-capturing approach can simulate the upstream-propagating shock generated upon the gate release in lock-exchange simulations. In addition, results of the hydraulic bore reflected off of an end wall also compare well to previous shock-fitting approaches.

- A new leading edge BC solution alternative was proposed [Hatcher and Vasconcelos, 2014] that has consistent implementation for both one and two-layer SWE models. Continuity errors were consistently less than 1% with the proposed boundary condition (BC).

- MicroADV probes successfully measured the velocities at three different depths in each fluid layer. Depth-averaged MicroADV results were obtained by taking the arithmetic average of measured velocities at different depths, and results compare well with SWE models [Hatcher and Vasconcelos, 2013a]. The key discrepancy for SWE model results is with maximum velocities, which were underestimated. Model results using Benjamin's front condition indicated a good match for maximum velocities, but leading edge arrival times were significantly underestimated due to entrainment effects.

Leading edge BC solution alternatives were analyzed in [Hatcher and Vasconcelos, 2014] for constant-volume and density intrusion gravity currents in the second phase of this research. The three BC solution strategies (referred to as Grid-of-Characteristics (GOC), Specified-Time-Intervals (STI) and Dual-Cell (DC) approaches) constitute variations of solving flows at the leading edges of gravity currents. STI and GOC methods apply characteristic equations and Riemann invariants alongside a front condition that accounts for drag. The DC method enforces explicit mass and momentum conservation for two cells at the leading edge in addition to a front condition. The leading edge BC approaches were compared in terms of continuity errors and computational time. Also in this second phase [Hatcher and Vasconcelos, 2014], the applicability of SWE models is explored focusing on constant-volume currents. Model results were compared to [Marino et al., 2005] experiments and a 2D computational fluid dynamics (CFD) model that was developed in OpenFOAM using the $k-\epsilon$ (with wall functions) and $\overline{v^2}-f$ (without wall functions) turbulence models. A summary of the findings is provided below:

- All three front BC approaches performed reasonably well in terms of continuity errors with values consistently less than 3% for computational cells greater than 500. As expected, the GOC approach performed noticeably better than the STI method, which utilizes interpolation. Continuity error results with the DC approach were in between the MOC alternatives.

- For the computational time comparison, all of the methods were fairly efficient except at discretization sizes exceeding 1,000 cells in which the GOC approach performed poorly. For GOC cases with large computational sizes, the number of characteristic lines generated was excessive and deemed this BC method unreasonably calculation intensive. The STI approach was slightly more computationally efficient than the DC approach, but both methods performed well.

- Compared to [Marino et al., 2005] experiments and 2D Reynolds-Averaged-Navier-Stokes (RANS) constant-volume simulations, the SWE model performed fairly well in terms of the gravity current (GC) front trajectory with errors consistently less than 5 %. However, the GC depth near the head was not simulated accurately as the details of the head were not resolved. Each of the numerical methods was fairly accurate in predicting the front trajectory in the slumping stage, but the $\overline{v^2} - f$ model was clearly superior in the self-similar or unsteady flow stage. The one-layer SWE model and $k - \epsilon$ model predicted leading edge arrival times with similar accuracy with both models underpredicting front velocities.

- With computational efforts orders of magnitude smaller than even the simplest 2D-RANS alternatives, SWE models may constitute an attractive means to obtain large sets of modeling results if modeling objectives are focused on the description of GC trajectories or average depths.

The last stage of this research consisted of an integral model development that was used to simulate non-Boussinesq currents propagating in stormwater tunnels [Hatcher et al., 2014]. Model results performed well in comparison with air-water experiments conducted by [Chosie, 2013]. Two integral models were formulated, which are referred to as $M1$ and $M2$. $M1$ incorporates theory from [Benjamin, 1968] and [Wilkinson, 1982] and accounts for surface tension in addition to drag and pressure forces. $M2$ is formulated from a more sophisticated front condition presented in [Vasconcelos and Wright, 2008] accounting for the

hydraulic jump seen in these GC experiments. $M2$ does not account for surface tension. The conclusions for this last stage and the related work of [Chosie et al., 2014] are summarized below focusing on the numerical work:

- The celerity of discrete air pockets in stagnant flow conditions depended on air pocket volume, particularly for shallower slopes (below 0.5%), in agreement with [Benjamin, 1968] and [Wilkinson, 1982] observations. For stronger slopes, celerity values were not as dependent on initial pocket volume as air accumulation at the leading edge of the air pocket reduced differences on the pocket thickness.

- The celerity of the air pocket leading edge in horizontal and adverse slopes was accurately predicted by the summation of values observed in quiescent conditions and ambient flow velocities.

- Predictions of the air pockets leading edge coordinate yielded by proposed numerical models compared well with experiments. $M1$ consistently yielded better results than $M2$ regardless of flow condition. This difference was highlighted for large air pocket volumes and smaller ambient flows in which $M2$ did not perform well. Results converged for the numerical modeling alternatives in larger ambient flow cases.

Chapter 6

Future Work

Two-layer SWE formulations were proposed for Boussinesq gravity currents using conservative and divergent format with one model accounting for initial ambient motion. However, extensions to axisymmetric, non-Boussinesq, particle-driven and stratified gravity currents have not been proposed as well as gravity currents propagating over porous media. In addition, an extension to two dimensions would serve as an important contribution to the hydraulics community.

For non-Boussinesq gravity currents in closed conduits, the integral model proposed in this work is capable of simulating a large range of background flow velocities and air pocket volumes. However, the model is not applicable for sloped pipelines. To extend the integral model to incorporate slopes ($So \leq 0.02$), additional experiments are be required in which the shape of the GC front needs to be accurately measured to account for Buoyancy at the GC front. Moreover, this integral model could be utilized as a sub model in more sophisticated stormwater tunnel models that currently do not account for air pocket motion. The details of air pocket formation and collapse in closed conduits and this impact on gravity current propagation is left for future investigations.

Bibliography

[Adduce et al., 2012] Adduce, C., Sciortino, G., and Proietti, S. (2012). Gravity currents produced by lock-exchange: experiments and simulations with a two layer shallow-water model with entrainment. *J. Hydraulic Eng.*, pages 111–121.

[Baines et al., 1985] Baines, W. D., Rottman, J. W., and Simpson, J. E. (1985). The motion of constant-volume air cavities in long horizontal tubes. *J. Fluid Mech.*, 161:313–327.

[Benjamin, 1968] Benjamin, T. B. (1968). Gravity currents and related phenomena. *J. Fluid Mech.*, 31:209–248.

[Benkhaldoun et al., 2007] Benkhaldoun, F., Elmahi, I., and Seaid, M. (2007). Well-balanced finite volume schemes for pollutant transport on unstructured meshes. *J. Computational Physics*, 226(1):180–203.

[Bonnecaze et al., 1995] Bonnecaze, R. T., Hallworth, M. A., Huppert, H. E., and Lister, J. R. (1995). Axisymmetric particle-driven gravity currents. *J. Fluid Mech.*, 294:93–121.

[Chaudhry, 2008] Chaudhry, M. H. (2008). *Open-Channel Flow*. Springer, second edition.

[Chosie, 2013] Chosie, C. D. (2013). Investigation on the kinematics of entrapped air pockets in stormwater storage tunnels. Master's thesis, Auburn Univsersity.

[Chosie et al., 2014] Chosie, C. D., Hatcher, T. M., and Vasconcelos, J. G. (2014). Experimental and numerical investigation on the motion of discrete air pockets in pressurized water flows. *J. Hydraulic Eng.*, 140(8).

[Cunge et al., 1980] Cunge, J. A., Holly, F. M. J., and Verwey, A. (1980). *Practical Aspects of Computational River Hydraulics*. Pitman Publishing Ltd., London, UK.

[Dai, 2014] Dai, A. (2014). Non-boussinesq gravity currents propagating on different bottom slopes. *J. Fluid Mech.*, 741:658–680.

[Dalziel, 1993] Dalziel, S. B. (1993). Rayleigh-taylor instability: experiments with image analysis. *Dyn. Atmos. Oceans*, 20:127–153.

[Durbin, 1991] Durbin, P. A. (1991). Near-wall turbulence closure without daming functions. *Theoretical and Computational Fluid Dynamics*, 3(1):1–13.

[Durbin, 1995] Durbin, P. A. (1995). Separated flow computations with the k-epsilon-v-squared model. *AIAA*, 33:659–664.

[Elena and Vazquez-Cendon, 1999] Elena, M. and Vazquez-Cendon (1999). Improved treatment of source terms in upwind schemes for the shallow water equations in channels with irregular geometry. *J. Computational Physics*, 148(2):497–526.

[Falvey, 1980] Falvey, H. T. (1980). Air-water flow in hydraulic structures. *USBR Engineering Monograph*, (41).

[Firoozabadi et al., 2010] Firoozabadi, B., Afshin, H., and Bagerpour, A. (2010). Experimental investigation of turbulence specifications of turbidity currents. *J. Applied Fluid Mech.*, 3(1):63–73.

[Gallouet et al., 2003] Gallouet, T., Herard, J., and Seguin, N. (2003). Some approximate godunov schemes to compute shallow-water equations with topography. *Computers & Fluids*, 32:479–513.

[Gerber et al., 2011] Gerber, G., Diedericks, G., and Basson, G. R. (2011). Paricle image velocimetry measurements and numerical modeling of a saline density current. *J. Hydraulic Eng.*, pages 333–342.

[Glaister, 1988] Glaister, P. (1988). Approximate riemann solutions of the shallow water equations. *J. Hydraulic Res.*, 26.

[Goldman et al., 2014] Goldman, R., Ungarish, M., and Yavneh, I. (2014). Gravity currents with double stratification: a numerial and analytical investigation. *Environ. Fluid Mech.*, 14(2):471–499.

[Hacker et al., 1996] Hacker, J., Linden, P. F., and Dalziel, S. B. (1996). Mixing in lock-release gravity currents. *Dynamics of Atmospheres and Oceans*, 24:183–195.

[Hallworth et al., 1998] Hallworth, M. A., Hogg, A. J., and Huppert, H. E. (1998). Effects of external flow on compositional and particle gravity currents. *J. Fluid Mech.*, 359:109–142.

[Hatcher, 2012] Hatcher, T. M. (2012). A finite volume implementation of the shallow water equations for boussinesq gravity currents. Master's thesis, Auburn University.

[Hatcher et al., 2014] Hatcher, T. M., Chosie, C. D., and Vasconcelos, J. G. (2014). Modeling the motion and spread of air pockets within stormwater sewers. *Journal of Urban Water Systems and Watershed Modeling*, 22.

[Hatcher and Vasconcelos, 2013a] Hatcher, T. M. and Vasconcelos, J. G. (2013a). Finite-volume and shock-capturing shallow water equation model to simulate boussinesq-type lock-exchange flows. *J. Hydraulic Eng.*, 139(12):1223–1233.

[Hatcher and Vasconcelos, 2013b] Hatcher, T. M. and Vasconcelos, J. G. (2013b). A finite volume, two-layer shallow water equation model to simulate gravity currents with ambient crossflows. *In World Environmental and Water Resources Congress 2013*, pages 1629–1637. ASCE.

[Hatcher and Vasconcelos, 2014] Hatcher, T. M. and Vasconcelos, J. G. (2014). Alternatives for flow solution at the leading edge of gravity currents using the shallow water equations. *J. Hydraulic Res.*

[Hogg et al., 2005] Hogg, A. J., Hallworth, M. A., and Huppert, H. E. (2005). On gravity currents driven by constant fluxes of saline and particle-laden fluid in the presence of a uniform flow. *J. Fluid Mech.*, 539:349–385.

[Huppert and Simpson, 1980] Huppert, H. E. and Simpson, J. E. (1980). The slumping of gravity currents. *J. of Fluid Mech.*, 99:785–799.

[Klemp et al., 1994] Klemp, J. B., Rotunno, R., and Skamarock, W. C. (1994). On the dynamics of gravity currents in a channel. *J. Fluid Mech.*, 269:169–198.

[Lai, 1988] Lai, C. (1988). Comprehensive method of characteristics models for flow simulation. *J. Hydraulic Eng.*, 114(9):1074–1097.

[Li and McCorquodale, 1999] Li, J. and McCorquodale, A. (1999). Modeling mixed flow in storm sewers. *J. Hydraulic Eng.*, 125(11):1170–1180.

[Liang and Marche, 2009] Liang, Q. and Marche, F. (2009). Numerical resolution of well-balanced shallow water equations with complex source terms. *Advances in Water Resources*, 32(6):873–884.

[Lien and Kalitzin, 2001] Lien, F. and Kalitzin, G. (2001). Computations of transonic flow with the v2f turbulence model. *Int. Journal of Heat and Fluid Flow*, 22:53–61.

[Lowe et al., 2005] Lowe, R. J., Rottman, J. W., and Linden, P. F. (2005). The non-boussinesq lock-exchange problem. part 1. theory and experiments. *J. Fluid Mech.*, 537:101–124.

[Macchione and Morelli, 2003] Macchione, F. and Morelli, M. A. (2003). Practical aspects in comparing shock-capturing schemes for dam break problems. *J. Hydraulic Eng.*, pages 187–195.

[Marino and Thomas, 2009] Marino, B. M. and Thomas, L. P. (2009). Front condition for gravity currents in channels of nonrectangular symmetric cross-section shapes. *ASME J. Fluids Eng.*, 131(5).

[Marino et al., 2005] Marino, B. M., Thomas, L. P., and Linden, P. F. (2005). The front condition of gravity currents. *J. Fluid Mech.*, 536:49–78.

[Martin, 1976] Martin, C. S. (Sept. 1976). Entrapped air in pipelines. In: BHRA (Ed.), *Proc. 2nd Int. Conf. Pressure Surges*. Bedford, England.

[Mehdizadeh and Firoozabadi, 2009] Mehdizadeh, A. and Firoozabadi, B. (2009). Simulation of a density current turbulent flow eploying different rans models: a comparison study. *J. of Scientia of Iranica*, 16(1):53–63.

[Mortensen et al., 2010] Mortensen, M., Reif, B. A. P., and Wasberg, C. E. (2010). Assessment of the finite volume method applied to the v2-f model. *International journal for numerical methods in fluids*, 63(4):495–516.

[Paez-Rivadeneira, 1997] Paez-Rivadeneira, D. L. (1997). *Density Current Propagation Over Horizontal Boundaries: An Experimental Study*. PhD thesis, University of Michigan.

[Peng and Lee, 2010] Peng, M. and Lee, C. B. (2010). Frontal instability of lock-exchange gravity currents. *Modern Physics Letters B*, 24(13):1369–1372.

[Pothof and Clemens, 2008] Pothof, I. and Clemens, F. (2008). Air migration analysis of the terror lake tunnel. *Proc. 11th Int. Conf. Urban Drainage, Edinburgh, Scotland*.

[Pozos et al., 2010] Pozos, O., Gonzalez, C., Giesecke, J., Marx, W., and Rodal, E. (2010). Air entrapped in gravity pipeline systems. *J. Hydraulic Res.*, 49(3):394–397.

[Robinson et al., 2013] Robinson, T. O., Eames, I., and Simons, R. (2013). Dense gravity currents moving beneath progressive free-surface water waves. *J. Fluid Mech.*, 725:588–610.

[Rottman and Simpson, 1983] Rottman, J. W. and Simpson, J. E. (1983). Gravity currents produced by instantaneous releases of a heavy fluid in a rectangular channel. *J. Fluid Mech.*, 135:95–110.

[Rotunno et al., 2011] Rotunno, R., Klemp, J. B., Bryan, G. H., and Muraki, D. J. (2011). Models of non-boussinesq lock-exchange flow. *J. Fluid Mech.*, 675:1–26.

[Shin et al., 2004] Shin, J., Dalziel, S., and Linden, P. F. (2004). Gravity currents produced by lock exchange. *J. of Fluid Mech.*, 521:1–34.

[Simpson, 1997] Simpson, J. E. (1997). *Gravity Currents In the Environment and the Laboratory*. Cambridge University Press.

[Simpson and Britter, 1979] Simpson, J. E. and Britter, R. E. (1979). The dynamics of the head of a gravity current advancing over a horizontal surface. *J. Fluid Mech.*, 94:477–495.

[Simpson and Britter, 1980] Simpson, J. E. and Britter, R. E. (1980). A laboratory model of an atmospheric mesofront. *Q. J. R. Met. Soc.*, 106:485–500.

[Sturm, 2010] Sturm, T. W. (2010). *Open Channel Hydraulics*. McGraw-Hill, second edition.

[Thomas et al., 2004] Thomas, L. P., Marino, B. M., and Linden, P. F. (2004). Lock-release inertial gravity currents over a thick porous layer. *J. Fluid Mech.*, 503:299–319.

[Toro, 2001] Toro, E. F. (2001). *Shock-Capturing Methods for Free-Surface Shallow Flows*. John Wiley and Sons.

[Townson, 1991] Townson, J. M. (1991). *Free-surface hydraulics*. Cambridge University Press.

[Ungarish, 2007] Ungarish, M. (2007). A shallow-water model for high-reynolds-number gravity currents for a wide range of density differences and fractional depths. *J. Fluid Mech.*, 579:373–382.

[Ungarish, 2008] Ungarish, M. (2008). Energy balances and front speed conditions of two-layer models for gravity currents produced by lock release. *Acta Mechanica 201*, (1-4):63–81.

[Ungarish, 2009] Ungarish, M. (2009). *An Introduction to Gravity Currents and Intrusions.* Chapman and Hall/CRC, first edition.

[Ungarish, 2011] Ungarish, M. (2011). Two-layer shallow-water dam-break solutions for non-boussinesq gravity currents in a wide range of fractional depth. *J. Fluid Mech.*, 675:27–59.

[Ungarish and Huppert, 2002] Ungarish, M. and Huppert, H. E. (2002). On gravity currents propagating at the base of a stratified ambient. *J. Fluid Mech.*, 458:283–301.

[Ungarish and Huppert, 2004] Ungarish, M. and Huppert, H. E. (2004). On gravity currents propagating at the base of a stratified ambient: effects of geometrical constraints and rotation. *J. Fluid Mech.*, 521(69-104).

[Ungarish and Zemach, 2005] Ungarish, M. and Zemach, T. (2005). On the slumping of high reynolds number gravity currents in two-dimensional and axisymmetric configurations. *European J. Mech. B/Fluids*, 24:71–90.

[Vasconcelos, 2005] Vasconcelos, J. G. (2005). *Dynamic approach to the description of flow regime transition in stormwater systems.* PhD thesis, University of Michigan.

[Vasconcelos and Wright, 2006] Vasconcelos, J. G. and Wright, S. J. (2006). Improved simulation of flow regime transition in sewers - two-component pressure approach. *J. Hydraulic Eng.*, 132(6):553–562.

[Vasconcelos and Wright, 2008] Vasconcelos, J. G. and Wright, S. J. (2008). Mechanisms for air pocket entrapment in stormwater storage tunnels. *J. Hydaulic. Eng.*, 134(7):984–992.

[von Karman, 1940] von Karman, T. (1940). The engineer grapples with nonlinear problems. *Bull. M. Math Soc.*, 46:615–683.

[Wilkinson, 1982] Wilkinson, D. L. (1982). Motion of air cavities in long horizontal ducts. *J. Fluid Mech.*, 118:109–122.

[Wright and Paez-Rivadeneira, 1996] Wright, S. J. and Paez-Rivadeneira, D. (1996). Density intrusions with large relative thickness. *Dynamics of Atmospheres and Oceans*, 24:129–137.

[Zhou et al., 2002] Zhou, F., Hicks, F., and Steffler, P. (2002). Transient flow in a rapidly filling horizontal pipe containing trapped air. *J. Hydraulic Eng.*, 128(6):625–634.

Chapter 7

Appendices

7.1 Journal publications and conference presentations

Journal Publications:

- Hatcher, T. M., Chosie, C. D., and Vasconcelos, J. G. (2014). Modeling the motion and spread of air pockets within stormwater sewers. *Journal of Urban Water Systems and Watershed Modeling*, 22.

- Chosie C. D., Hatcher, T. M., and Vasconcelos, J. G. (2014). Experimental and numerical investigation on the motion of discrete air pockets in pressurized water flows. *J. Hydraulic Eng.*, 140(8).

- Hatcher, T. M. and Vasconcelos, J. G. (2013). Alternatives for flow solution at the leading edge of gravity currents using the shallow water equations. *J. Hydraulic Res.*

- Hatcher, T. M. and Vasconcelos, J. G. (2013). Finite-volume and shock-capturing shallow water equation model to simulate Boussinesq-type lock-exchange flows. *J. Hydraulic Eng.*, 139(12):1223-1233.

Conference presentations:

- Hatcher, T. M. and Vasconcelos, J. G. (2014). Experimental study on scale effects in surges caused by sudden air pocket entrapments. In *World and Water Resources Congress 2014@ sWater Without Borders*. ASCE, pages 1282-1291.

- Hatcher, T. M. and Vasconcelos, J. G. (2013). A finite volume, two-layer shallow water equation model to simulate gravity currents with ambient crossflows. *In World Environmental and Water Resources Congress 2013*. ASCE, pages 1629-1637.

- Hatcher, T. M., KC, M., Vasconcelos, J. G., and Fang, X. (2012). A comparison between numerical modeling approaches for the simulation of gravity currents. *In World Environmental and Water Resources Congress 2012@ sCrossing Boundaries*. ASCE, pages 1108-1118.

7.2 Education background

09/2010-09/2012 M.S. Auburn University, Auburn, Alabama. Civil Engineering.

09/2007-05/2010 B.S. Florida Atlantic University, Boca Raton, Florida. Civil Engineering.